Accepted to Phys. Fluids 10.1063/5.0120201

On the Effect of Flow Regime and Pore Structure on the Flow Signatures in Porous Media

Mehrdad Vasheghani Farahani, Mohaddeseh Mousavi Nezhad

Porous Materials and Process Modelling Research Group, School of Engineering, University of Warwick, Coventry, UK, CV4 7AL

Corresponding author: Mohaddeseh Mousavi Nezhad (M.Mousavi-Nezhad@warwick.ac.uk)

Abstract

In this study, lattice Boltzmann method (LBM) is utilised for three-dimensional simulation of fluid flow through two porous structures, consisting of grains with the same diameter: (i) a homogeneous porous domain, in which the grains are placed with a simple cubic packing configuration, and (ii) a randomly-packed porous domain. An ultra-fine mesh size is considered to perform the simulations in three orders of magnitude of Reynolds number (Re), covering laminar to turbulent flow regimes, and capture different flow signatures. Pore velocity fields are derived, and their sample probability density functions (PDF) are analysed versus time to investigate the dynamics of the flow. The analysis of the PDFs clearly shows that stagnant zones play a significant role in the formation of the pore flow fields, manifested by multimodal PDFs, and the distribution of the velocities in porous media at various Re cannot be characterised by a single PDF model regardless of the pore structure. While the velocities at the stagnant regions and in the vicinity of the solid boundaries are primarily affected by the viscous forces and exhibit a power-law PDF at different Re, the velocities in the main (preferential) flow pathways away from the boundaries are shown to be influenced by the inertial forces, hence having an exponential PDF when Re is low. At high Re, however, depending on the tortuosity of the porous structure, the velocities may exhibit an exponential or even Laplace PDF.

Keywords: Pore-scale modelling, Lattice Boltzmann Method, Probability density function.

1. Introduction

Porous systems are found in various scientific fields and engineering applications such as oil and gas recovery, geological storage of CO_2 and H_2, geothermal energy storage, groundwater remediation, chromatography, exploitation of unconventional reservoirs, and fuel cells [1–5]. Such a wide array of applications necessitates a profound understanding of heat and mass transfer phenomena occurring in pore space, which are associated with single or multiphase fluid flow. Given the flow in porous media is substantially influenced by its complex disordered nature, the physics of flow is essential to be characterised to achieve a desired flow rate-pressure drop response. This is of particular importance when the flow is required to be tailored for a given application [6].

Despite its micro-scale characteristics, fluid flow in porous media has been typically described using Darcy's law in various scientific and industrial applications, a macro-scale approach with several simplifying assumptions, which neglects local aspects such as pore-scale flow variations within the interstitial regions and may even fail to accurately predict the transport properties under the high-flow conditions within intricate pore space [7–9]. On the other side of the coin, several experimental and modelling studies substantiated that the local flow dynamics can significantly influence transport phenomena such as solute transport, mixing, and heat transfer in pore space at different flow regimes [10–14], necessitating the incorporation of the pore-scale characteristics into the effective transport properties. Therefore, it is of utmost priority to investigate fluid flow and the evolution of the velocity fields at pore level [15]. These investigations are essential to be conducted in correlation with the inertia effect, i.e. Reynolds number (Re), and geometric heterogeneity of porous media as they directly control the flow signatures within pores and also the local deviations from Darcy's law [16,17]. The pore-scale insights are of particular importance at high-velocity conditions, where the local level of turbulence impacts the transport of scalar properties and improves heat and mass transfer [18,19]. This enhancement is welcomed in many industrial applications and widely investigated by scholars, a comprehensive review in this regard can be found elsewhere [20].

Pore-scale insights into the flow characteristics can be obtained by both experimental and modelling studies. The experimental approaches usually utilise optical techniques such as micro-particle image velocimetry (PIV) for the visualisation of flow in pore space [13,21]. X-ray CT imaging and magnetic resonance imaging (MRI) are the other advanced techniques for the visualisation of fluid flow in porous media [22,23]. The experimental studies are crucial for not only shedding light on the dynamics of flow in porous structures but also providing an experimental database to support the verification and improvement of numerical approaches [21]. However, there are some limiting factors hindering their extensive application in different disciplines. For instance, the majority of the experimental methods require advanced high-cost facilities (high-speed cameras, illumination sources, X-ray micro-CT imaging systems, etc.), which are not readily available. Strict health and safety regulations must also be taken into consideration in laboratory regarding the reactivity and hazard level of the fluids and apparatuses [24]. Apart from these concerns, there are some inherent technical limitations about the spatiotemporal measurement capabilities of these methods, making their application merely suitable for the pore-scale studies where the flow is slow and/or the pore sizes are large enough to be observed. In addition, they often provide access to the velocity data in two-dimensional (2D) planar sheets which makes it difficult to probe the three-dimensional (3D) flow hence limited statistics can be extracted [7]. Recent advances in stereo-PIV and synchrotron X-ray micro-CT imaging enable four-dimensional (4D) visualisation of the laminar flow in porous structures [25–28]; however, higher measurement frequencies are required for the cases in which both spatial velocity fluctuations and local turbulence exist in pores.

Advances in computing capabilities have made it possible to use different pore-scale modelling approaches to study the dynamics of flow as well as transport properties at the pore level. The computational methods have shown a great potential for capturing complex flow signatures as well as local pore-scale variations arising from the navigation of tortuous pore space by the fluid and successfully applied for studying various pore-scale phenomena associated with fluid flow in both ideal and real porous media [29]. Pore-network modelling (PNM), as a less computationally demanding approach, has been successfully used for studying various transport phenomena in porous media such as single and multiphase flow, immiscible displacement, and solute transport [30]. Despite its extensive applications in digital rock physics, PNM does not account for the irregularities and geometric details of pore/throats for the sake of simplicity [31]. Thus, it cannot be applied to studies where detailed solid-fluid interactions and their influences on the transport properties and velocity variations are essential to be captured. Thanks to recent advances in high-performance computing, computational fluid dynamics (CFD) approaches have been successfully employed for numerical simulation of transport phenomena in porous media [29]. The continuum-scale CFD approaches, such as finite difference method (FDM), finite element method (FEM), and finite volume method (FVM), directly solve the governing equations to characterise the pore-scale transport and obtain the macroscopic transport properties such as absolute/relative permeability [5,11,32,33]. However, the application of these methods is fairly challenging in complex geometries, particularly at high Re, due to their inherent high computational costs and intractability in capturing the fluid-solid interactions [34]. Among the CFD approaches, lattice Boltzmann method (LBM) is a well-suited approach for pore-scale simulations primarily owing to its great strength in treating complex irregular solid boundaries and its parallel computing advantages over the other continuum-scale methods [35,36]. With an acceptable computational cost, LBM can provide accurate spatiotemporally resolved flow properties at the regions away from solid boundaries hence has a great potential to be applied for studies with interest in the characterisation of velocity fluctuations in the pores.

It is a given that pore-scale transport is markedly influenced by the geometric characteristics of porous structures [37]. However, a common approach for the simulation of flow and investigation of transport mechanisms in porous media is to adopt regular geometries such as Simple Cubic (SC) and Body-Centred Cubic (BCC) packing structures [38–40]. Although these regular geometries help with incorporating the fluid-solid interactions and can be considered as alternatives to real pore structures when they are not available, there is still a big concern about their capability to account for the complexities arising from the heterogeneous and tortuous nature of real porous media and the effect of the solid-fluid interactions on the flow signatures. Therefore, it is essential to understand the differences of the flow properties in ordered ideal structures with those of disordered real porous media. These insights are necessary when studying dispersion and mixing in different porous structures due to the fact that the transport of the scalar properties is fundamentally controlled by the distribution of the pore velocities [41]. In other words, modelling mixing in porous media requires a profound understanding of the probability density function (PDF) of the velocities in correlation with the structural heterogeneity [42], particularly at the low-velocity range as it governs the possible anomalous nature of transport in porous media. This makes it necessary to investigate the velocity distribution in two physically distinct regimes: small and high velocities [41]. The previous experimental and numerical studies show that the small velocities – found in dead-end pores and the volumes in the proximity of the fluid-solid interfaces – should be described by a power-law PDF model while the high velocities – found in the main pathways – exhibit an exponential PDF [43]. However, there are still uncertainties about the velocity PDFs. For instance, some studies reported increasing power-law PDFs in the low-velocity regions [44,45], contradicting the flat or even decreasing behaviours found in the other works [42,46–48]. Such inconsistencies indicate that active debate still remains about the nature of the velocity PDFs in porous media.

In this work, we utilise LBM for 3D simulation of single-phase fluid flow through both regularly- and irregularly-packed porous media. The main objective of this study is to shed light on the dependency of the flow signatures on Re and tortuosity of the pore structure at both local and global scales. Given the low and high Re flows in porous media occur in various environmental, geoscience, and industrial applications [49,20,50], the simulations are carried out at three orders of magnitude of Re, covering Stokes, laminar, and turbulent flow regimes. The statistical analysis of the simulation results will also help with providing fundamental insights regarding the effect of the pore structure and geometric characteristics on the flow features at various flow regimes.

2. Method

In this section, a detailed description is provided regarding the geometry of the porous structures as well as the governing flow equations, boundary conditions, and the numerical method employed to solve the equations for obtaining the evolution of the pore-scale velocity fields.

2.1 Governing equations

Fluid flow in the pore space can be described by the incompressible continuity and Navier-Stokes equations:

$$\nabla \cdot \vec{u} = 0 \tag{1}$$

$$\frac{\partial \vec{u}}{\partial t} + (\vec{u}.\nabla)\vec{u} = -\frac{1}{\rho}\nabla p + \nu \nabla^2 \vec{u} \tag{2}$$

where $\vec{u} = (u_x, u_y, u_z)$ is the fluid velocity, p is the pressure, and ν is its dynamic viscosity. In this work, LBM is employed to conduct the fluid flow simulations. LBM is a discrete form of the continuous kinetic Boltzmann equation with discretised time and space coordinates [35]. The solution algorithm assumes the fluid as a large number of randomly moving fictive particles that exchange momentum (and energy for the non-isothermal problems) through collision and streaming processes, evolving the density of the fluid $\rho(\vec{x}, t)$, for $\vec{x}$ the position and t the time [51]. A finite set of vectors are used to limit the space coordinate and construct a lattice to denote the directions where the fluid particles can move. It is common to classify the lattice models as “DnQm” where “Dn” and “Qm” are “n space dimensions” and “m discrete velocity vectors” in the model [52]. In this study, we use D3Q19 lattice model, in which each lattice node is surrounded by 18 neighbouring nodes.

Considering an Eulerian basis $\vec{x} = (x,\ y,\ z)$ and assuming i (0, …, 18) as the direction available for the fluid movement in the D3Q19 lattice model, the particle distribution function $f_i(\vec{x},\ t)$ is defined as the fraction of the density with the discrete lattice velocity $\vec{c}_i$ at location $\vec{x}$ and time t. The lattice Boltzmann equation (LBE):

$$f_i(\vec{x} + \vec{c}_i \Delta t, t + \Delta t) = f_i(\vec{x}, t) + \Omega_i \tag{3}$$

predicts the space and time evolution of the particle distribution functions that collide and stream along the direction i [53]. The numerical scheme is divided into collision and streaming steps:

$$\begin{aligned} f_i^*(\vec{x}, t) &= f_i(\vec{x}, t) + \Omega_i \\ f_i(\vec{x} + \vec{c}_i \Delta t, t + \Delta t) &= f_i^*(\vec{x}, t) \end{aligned} \tag{4}$$

where $f_i^*(\vec{x}, t)$ is the post-collision particle distribution function and Ω_i is the collision operator. Owing to its computational efficiency and reliability [54], Bhatnagar–Gross–Krook (BGK) collision operator is used in this work:

$$\Omega_i = \frac{1}{\tau}\left(f_i^{eq}(\vec{x}, t) - f_i(\vec{x}, t)\right) \tag{5}$$

in which τ is the lattice relaxation time and $f_i^{eq}(\vec{x}, t)$ is the equilibrium distribution function:

$$f_i^{eq}(\vec{x},t) = \omega_i \rho(\vec{x},t)\left[1 + \frac{\vec{c}_i.\vec{u}}{c_s^2} + \frac{(\vec{c}_i.\vec{u})^2}{2c_s^4} - \frac{\vec{u}.\vec{u}}{2c_s^2}\right] \tag{6}$$

In Eq.(6), $c_s = 1/\sqrt{3}$ is the lattice sound speed and ω_i is a fixed weighting factor in the direction i:

$$\omega_i = \begin{cases} 1/3 & i = 0 \\ 1/18 & i = 1-3 \; and \; 10-12 \\ 1/36 & i = 4-9 \; and \; 13-18 \end{cases} \tag{7}$$

The density and velocity could be related to the distribution functions by:

$$\rho = \sum_i f_i \qquad \vec{u} = \frac{1}{\rho}\sum_i f_i \vec{c}_i \tag{8}$$

Through Chapman-Enskog expansion, the governing continuity and Navier–Stokes equations can be recovered from the LBM algorithm and the fluid kinematic viscosity ν can be related to the lattice relaxation time via:

$$\nu = \frac{1}{3}\left(\tau - \frac{1}{2}\right) \tag{9}$$

More details regarding LBM can be found elsewhere [35].

We adopt D3Q19-BGK-LBM implemented in OpenLB (https://www.openlb.net/) to conduct the fluid flow simulations and obtain the flow fields [55]. Poiseuille flow through a cylindrical tube as a well-known flow problem having exact analytical solution was utilised to validate the developed code; see Appendix A for further details. A constant velocity boundary condition is imposed at the inlet surface and a constant pressure boundary condition is prescribed at the outlet surface. No-slip bounce-back boundary condition is also considered at the outer walls of the domain in the y- and z-directions as well as the fluid-solid interfaces. For a given simulation case, a constant inlet velocity $\vec{u}_{in} = (u_{in},\ 0,\ 0)$ is imposed for all the inlet boundary nodes (shown in Yellow in Figure 1) and the evolution of the velocity fields within the pore space is monitored versus time until the flow becomes fully developed and converged. Having u_{in}, Re can be calculated as:

$$Re_p = \frac{(u_{in}/\phi)D_p}{\nu} \tag{10}$$

In Eq.(10), u_{in}/ϕ is the interstitial velocity, which is used for normalising the velocity magnitudes and its components throughout this study. It should be noted that the simulation results include the velocity magnitude and its components in the x, y, and z-directions for each lattice point at different time steps; the analysis of which was carried out using ParaView [56].

At the steady state conditions, the relative variations of the velocities are expected to be zero throughout the computational domain, which would be ideal because of the numerical errors and the possibility of the presence of the spatiotemporal evolving flow signatures, particularly at high Re. Therefore, the convergence of the solution is monitored by finding the average normalised velocity magnitudes at three different planar sheets perpendicular to the imposed flow direction (x-direction), one at the middle and the other two at the first and third quarters of the domain and calculating its relative variation over time. The solution is considered to be converged when the relative variations of the average normalised velocity magnitudes become less than 5%. It should be noted that the simulation continues after the convergence is achieved in order to capture any spatiotemporal evolution of the flow signatures within the pore space.

2.2 Geometry of the porous structures

We study the fluid flow in two cubic porous media with the size of 200^3 μm^3, consisting of spherical grain particles with the same diameter (D_p) of 100 μm, as illustrated in Figure 1. The porous structures both have the porosity (ϕ) of ~36%, calculated via obtaining the number of their fluid and solid voxels. The first structure shown in Figure 1-(a) is a regular porous domain, in which the grains are placed next to each other with the SC packing configuration. The other structure shown in Figure 1-(b) is a randomly-packed porous domain taken from a 600^3 μm^3 beadpack image. The beadpack image is created and segmented by Prodanović and Bryant [57] to represent the experimental measurements of the coordinates of the centres of equally-sized spherical grain particles obtained by Finney [58]. It has the voxel size, porosity, and absolute permeability of 2 μm, 0.359 and 5.43×10^{-12} m^2 [5], respectively, been shown to be representative of packed-bed porous media, and used by scholars to investigate pore-scale transport in the other studies [8,59,60].

As the randomly-packed structure is sampled from the beadpack image, it is essential to investigate whether it is still representative of packed-bed porous media. There are different analysis techniques such as re-running the simulations where the primary flow direction is changed and obtaining the corresponding permeabilities [61], or comparing the petrophysical properties such as porosity and permeability of the sampled medium with those of the original structure. The porosity and permeability of the randomly-packed sample are 0.36 and 5.01×10^{-12} m^2, quite close to those reported for the beadpack image in the literature, showing that the randomly-packed structure can be representative of packed-bed porous media.

We consider a lattice mesh size of 0.4 μm for the discretisation of the pore space, which is 5 times smaller than that of the voxels in the beadpack image. As a common approach for maintaining the stability of the solution in LBM at high-velocity conditions is to refine the lattice mesh [62], the ultra-fine mesh size enables us to not only run the simulations at high Re but also capture the spatially-resolved complex flow signatures.

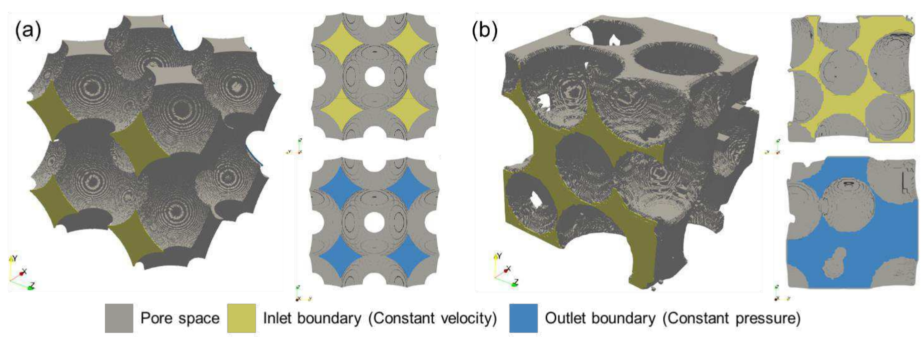

Figure 1. Geometries of the (a) regular SC-packed and (b) irregular randomly-packed porous structures. Fluid flows in the x-direction and constant velocity (Yellow) and pressure (Blue) boundary conditions are considered at the inlet and outlet boundaries, respectively.

3. Results

3.1 The evolution of the PDF of the velocity fields

3.1.1 SC-packed porous medium

The fluid flow simulations were conducted for the SC-packed porous medium, the pore velocity magnitudes and components both along and transverse to the imposed flow direction were extracted for each lattice point, normalised against the interstitial velocity, and their sample PDF were plotted at Re of 0.98, 9.81, and 98.14 in Figure 2, Figure 3, and Figure 4, respectively. In these figures, the simulation times (t) were normalised against the total simulation time (t_{Total}):

$$t^* = \frac{t}{t_{Total}} \tag{11}$$

The spatial distribution and streamlines of the velocity field at t_{Total} were also depicted for each Re to assist with the analysis of the PDFs. It should be emphasised that the effect of the inlet (constant velocity) boundary on the PDF of the velocities was minimised by excluding the first quarter of the flow domain when extracting the velocity data. Table 1 summarises the average normalised velocity magnitudes at the middle planar sheet perpendicular to the x-direction, used to check the convergence of the solution (as demonstrated earlier), assisting with the understanding of the evolution of the velocity fields at different Re and times. The PDFs can be also found in Supplementary Material.

Table 1. The average normalised velocity magnitudes at the middle planar sheet perpendicular to the x-direction in the SC-packed porous medium at different Re and normalised simulation times.

No.	Re	Average Normalised Velocity (-)				
		$t^* = 0.2$	$t^* = 0.4$	$t^* = 0.6$	$t^* = 0.8$	$t^* = 1.0$
1	0.98	0.95	1.31	1.53	1.57	1.60
2	9.81	1.52	2.03	1.77	1.58	1.60
3	98.14	1.07	1.53	1.71	1.71	1.67

According to Table 1 and Figure 2, the convergence of the solution at Re = 0.98 is achieved in $t^* = 0.6$, and the flow becomes fully developed throughout the domain. However, there are still small discrepancies in the tail of the PDFs (<0.5% of the velocity data), which could be attributed to the ultimate development of the velocity field at the centre of the pore throats with the highest velocities (Figure 2-(e)).

In Figure 2-(a), the PDF of the normalised x-direction velocity can be divided into three main parts: (i) the negative velocities, (ii) the positive velocities lower than 1.47, and (iii) the positive velocities higher than 1.47. The presence of the negative x-direction velocities in the non-tortuous SC-packed porous medium – in which there is no pathway opposite to the imposed flow direction hence no backflow – can only be due to the formation of the recirculating flow structures aligned with the imposed flow direction. Therefore, as no negative velocity is observed in Figure 2-(a) after the convergence of the solution, there must not be any flow recirculation in the imposed flow direction, suggesting the dominance of the Stokes (creeping) flow in the pore space, which is expected at low Re [63]. However, a number of small recirculating flows perpendicular to the imposed flow direction can be still spotted at the wake of the grain particles (see Figure 2-(e)). These regions are referred to as the stagnant zones, where the velocities are much lower than those at the main flow pathways hence the fluid flow is driven dominantly by the viscous forces [64]. Therefore, as the fluid layers of lower energies flow inside these regions, they experience more details of the landscape at the fluid-solid interface, and viscous momentum is transmitted laterally across successive laminae of the fluid, generating small-scale and low-energy recirculating flow structures [65]. The separation of the positive normalised velocities at 1.47 suggests the presence of two distinct flow signatures, which cannot be characterised with a single PDF. In Figure 2-(b) and (c), a perfectly symmetrical distribution is observed for the velocity components in the y- and z-directions, which is expected owing to the geometrical symmetry of the SC-packed domain in both directions. Interestingly, two different flow signatures are observed in these directions, separated at ~0.1. Therefore, the distribution of the velocities lower than 0.1 should be described differently than the higher velocities. Such distinctive flow signatures are expected primarily because the flow characteristics in the main pathways away from the solid boundaries with high velocities (the high-velocity zones) are controlled by the inertial forces while the viscous forces are dominant in the stagnant regions as well as the vicinity of the solid boundaries at the main flow pathways (the low-velocity zones) [66]. Here, we emphasise that the log-

log plot of the PDF of the velocity components has been also analysed to confirm the distinctive velocity values.

The velocity PDFs in Figure 2-(d) exhibit two different signatures, similar to what observed for the positive velocities in the x-direction, and the separation point is 1.47. For the velocities higher than this distinctive value, an exponential decay can be fitted to the velocity distribution, which has been already observed in the other numerical and experimental studies [7,67,41,68]. In fact, the exponential function can be used to characterise the flow in the main pathways where the inertial forces are dominant. The inset in Figure 2-(d) depicting the log-log PDF plot of the normalised velocities confirms that the velocity in the low-velocity zones should be characterised with a power-law PDF model instead.

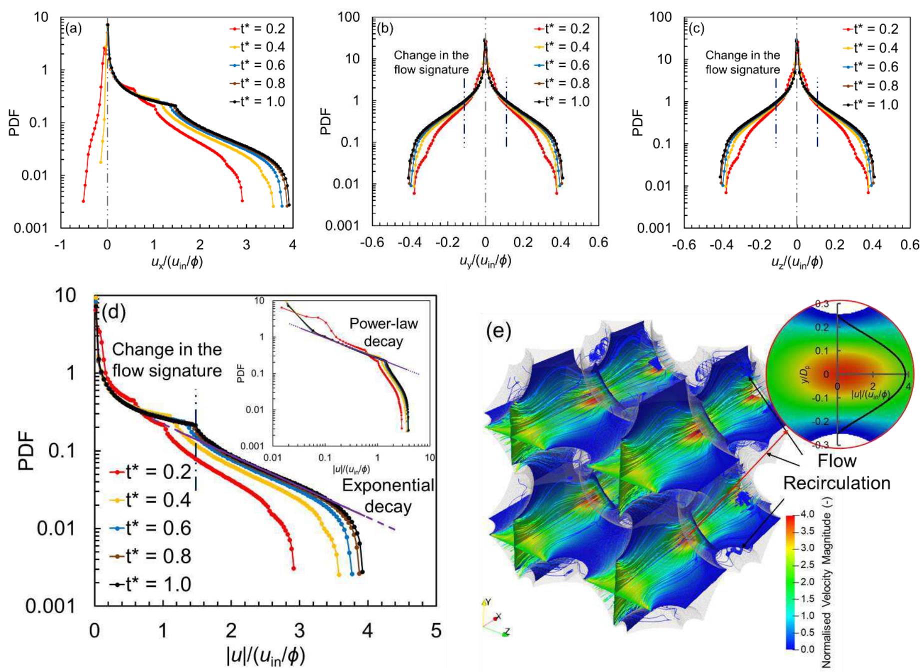

Figure 2. Temporal evolution of the normalised velocity fields within the SC-packed porous structure at Re = 0.98: (a-d) log-linear PDF plot of the normalised velocity magnitude and its components in the x, y, and z-directions, and (e) the spatial distribution and streamlines of the velocity field at $t^* = 1.0$. The inset in (d) is the log-log plot of the PDF of the normalised velocity magnitude.

According to Table 1 and Figure 3, the solution convergence at Re = 9.81 is obtained in $t^* = 0.8$, later than the convergence time of the previous case. The main reason for the delay in the convergence of the velocity is the formation of the recirculating flow structures oriented in the imposed flow direction at the stagnant regions. This can also be confirmed by investigating the PDF of the x-direction velocity component (Figure 3-(a)), where almost 5% of the velocity data become negative after $t^* = 0.6$. The recirculating flow structures could be of particular interest when investigating the transport of the scalar properties such as chemicals through porous media [69]. It should be noted that the presence of the recirculating flow structures at the stagnant regions of regularly-packed porous media as well as their dependence on the pore structure have been experimentally investigated at high Re in the other studies [70–72]. The ultra-fine mesh size considered in this study assisted us with capturing them even at smaller Re and confirming their size and orientation dependence on the velocity of the fluid flowing within the system.

The PDFs of the normalised velocities at Re = 9.81 and $t^* = 1.0$ in Figure 3-(a) to (d) are generally similar to the ones at Re = 0.98; however, they exhibit some distinguished features. Apart from the presence of the negative x-direction velocities and recirculating flows, which were discussed above, a clear separation of the velocity distributions in the y- and z-directions can be seen at the normalised value of ~0.2. Besides, the distinctive point of the normalised velocity magnitudes is ~1.8, which is higher than what captured in the previous case. This difference can be attributed to the size of the recirculating flow structures and the magnitude of the velocities in these regions. It can be seen in Figure 3-(e) that the recirculating flows are larger than those in Figure 2-(e), and they are extended from the stagnant regions to the main pathways hence influencing wider areas. Thus, the transmission of the viscous momentum across successive laminae of the fluid could even occur in the regions with higher velocities, which results in shifting the distinctive velocity to a higher value.

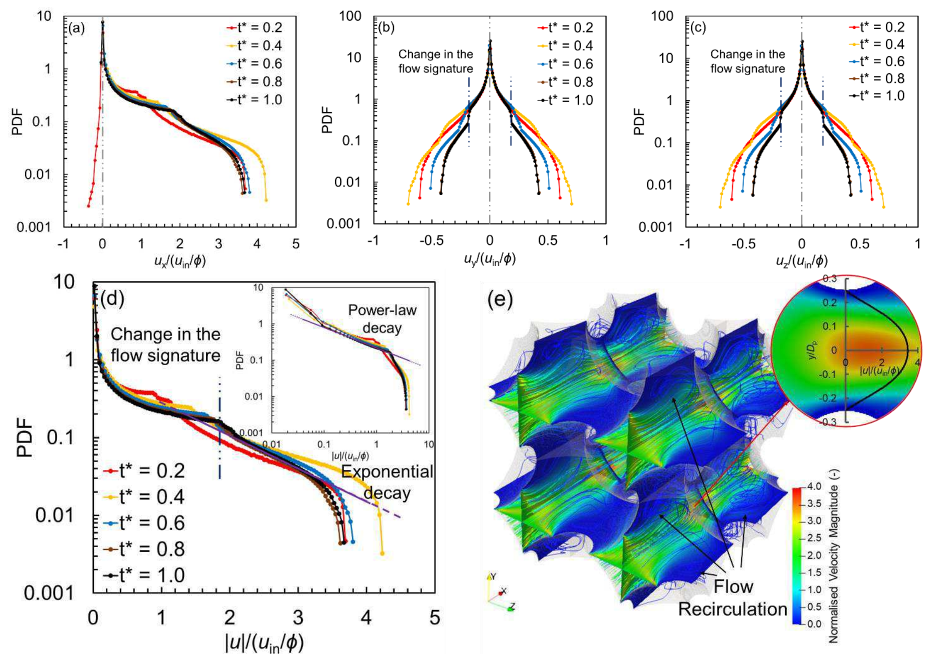

Figure 3. Temporal evolution of the normalised velocity fields within the SC-packed porous structure at Re = 9.81: (a-d) log-linear PDF plot of the normalised velocity magnitude and its components in the x, y, and z-directions, and (e) the spatial distribution and streamlines of the velocity field at $t^* = 1.0$. The inset in (d) is the log-log plot of the PDF of the normalised velocity magnitude.

The PDF of the velocity magnitude and its components at Re = 98.14 is illustrated in Figure 4. The solution convergence is obtained in $t^* = 0.8$, according to Table 1; however, there are still some differences in the tail of the PDF of the normalised velocity magnitude and its x-direction component (<2% of the velocity data). The highest velocities are only found at the converging/diverging region of the pore throats (see Figure 4-(e)); therefore, such differences could be due to the flow instabilities at these regions, a phenomenon captured experimentally at high Re in the other studies [26,6].

In Figure 4-(a), the PDF of the normalised x-direction velocity can be divided into three main parts: (i) the negative normalised velocities that are more than 23% of the x-direction velocity data, meaning the large-scale recirculating flow zones do exist in almost a quarter of the pore space (covering all the stagnant regions and extending into the main pathways), (ii) the positive normalised velocities lower than the distinctive value of 1.0 (the interstitial velocity), and (iii) the positive velocities higher than 1.0. The separation of the positive normalised velocities again confirms there are two distinctive flow signatures. However, the trend at the velocities higher than the distinctive velocity value is entirely different from what observed in Figure 2 and Figure 3, suggesting a new flow signature at the main pathways; this will be discussed in the next paragraph. In Figure 4-(b) and (c), a symmetrical distribution is observed for the velocity components in the y- and z-directions, and similar to the previous cases, the distribution of the velocity components lower than the distinctive value of 0.1 should be characterised differently from the higher velocity components in these two directions.

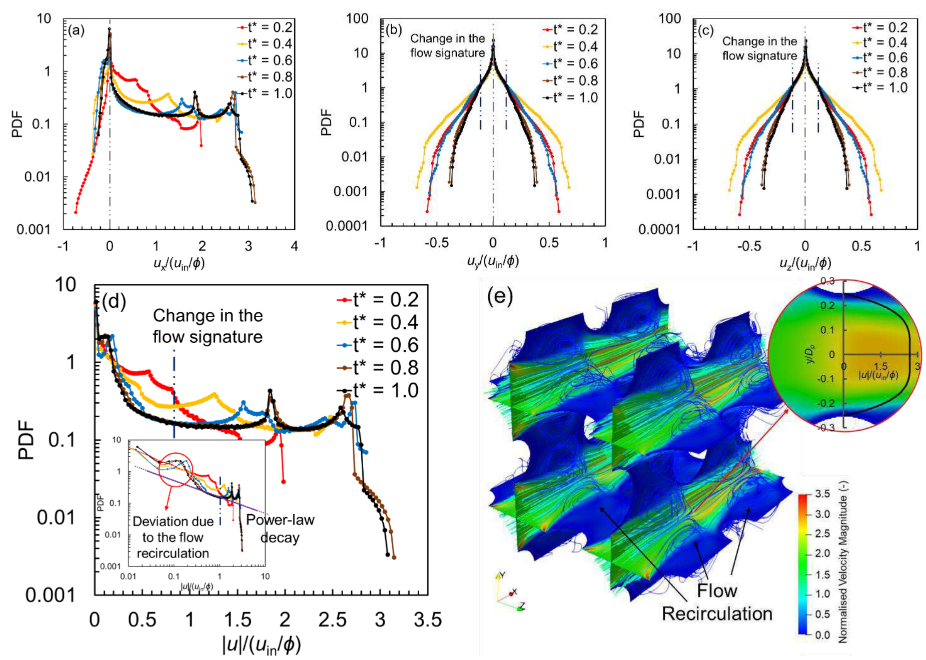

Figure 4. Temporal evolution of the normalised velocity fields within the SC-packed porous structure at Re = 98.14: (a-d) log-linear PDF plot of the normalised velocity magnitude and its components in the x, y, and z-directions, and (e) the spatial distribution and streamlines of the velocity field at $t^* =$ 1.0. The inset in (d) is the log-log plot of the PDF of the normalised velocity magnitude.

Given the imposed flow is in the x-direction, the PDF of the normalised velocity magnitude is quite similar to its x-direction component. According to the log-linear PDF plot in Figure 4-(d), the velocities higher than the interstitial velocity exhibit a Laplace PDF (with two distinguished location parameters of 1.84 and 2.58), which is entirely different from the exponential behaviour observed for the high velocities at lower Re. This interesting behaviour can be simply attributed to the fact that a fluid jet enters the pore space at such a high Re and flows through the main pathways. Since the pore structure is regular and non-tortuous, there is no obstacle to change the flow direction. As a result, the flow keeps being fully turbulent within these regions and the velocity profile would not become parabolic, similar to the turbulent velocity profile in pipes [73]. Therefore, the PDF of the velocity at the main pathways with the turbulent flow regime changes to the Laplace with the location parameter of 2.58.

It should be noted that the Laplace model for the high velocities may not be necessarily observed in the other porous media as the pore structure can highly influence the trajectory of the main flow pathways, this will be discussed in Section 3.1.2. The reason for having another location parameter at 1.84 is that the turbulent flow in the pores located closer to the inlet boundary is still influenced by the inlet boundary conditions, resulting in a similar distribution but with a lower location parameter, which could be of particular interest for the studies investigating the effect of the boundary flow in transport phenomena in porous media. According to the log-log PDF plot in Figure 4-(d), the velocities lower than 1.0 can be still characterised with a power-law PDF model similar to the results at low Re, confirming the presence of a viscous (laminar) flow regime in the vicinity of the solid boundaries with no-slip boundary conditions, surrounding the turbulent flow regions. The deviations from the power-law decay around the normalised velocity of 0.1 are also caused by the recirculating flows.

As discussed above, the PDF of the velocity magnitude as well as its components in the SC-packed porous medium must be quantified with two models regardless of Re. Table 2 summarises the type and parameter(s) of the PDF models fitted to the distribution of the normalised velocity magnitudes at both low- and high-velocity zones. As can be seen, while the exponent of the power-law functions in the low-velocity regions (k) does not exhibit any clear sensitivity to Re, the rate parameter of the exponential functions in the high-velocity regions (λ) becomes higher when Re increases; a direct proportionality observed at low Re in the other studies [7,59].

Table 2. Summary of the type and parameter(s) of the models fitted to the PDF of the velocity magnitudes in the SC-packed porous structure. u^* here the normalised velocity magnitude, $|u|/(u_{in}/\phi)$.

No.	Re	PDF model		Distinctive normalised velocity magnitude (-)
		Low-velocity zones	High-velocity zones	
1	0.98	$PDF \propto u^{*-k}, k = 0.571$	$PDF \propto e^{-\lambda u^*}, \lambda = 0.936$	1.47
2	9.81	$PDF \propto u^{*-k}, k = 0.559$	$PDF \propto e^{-\lambda u^*}, \lambda = 1.140$	1.80
3	98.14	$PDF \propto u^{*-k}, k = 0.623$	$PDF \propto e^{-\frac{\lvert u^*-\mu \rvert}{b}}, \mu = 1.84, 2.58, b = 3.44, 1.21$	1.00

3.1.2 Randomly-packed porous medium

We conducted the fluid flow simulations for the randomly-packed porous medium at Re of 1.16, 11.59, and 115.85, extracted the velocity magnitudes and its components, normalised them against the interstitial velocity, and plotted their sample PDF evolutions at various times in Figure 5, Figure 6, and Figure 7, respectively, together with the spatial distribution and streamlines of the velocity field at t_{Total}. The average normalised velocity magnitudes at the middle planar sheet perpendicular to the x-direction, which were used to check the convergence of the solution, are provided in Table 3. These velocities help with the analysis of the evolution of the velocity fields at different Re and times. The PDFs are also available in Supplementary Material.

Table 3. The average normalised velocity magnitudes at the middle planar sheet perpendicular to the x-direction in the randomly-packed porous medium at different Re and normalised simulation times.

No.	Re	Average Normalised Velocity (-)

		$t^* = 0.2$	$t^* = 0.4$	$t^* = 0.6$	$t^* = 0.8$	$t^* = 1.0$
1	1.16	0.81	1.08	1.16	1.17	1.18
2	11.59	1.20	1.39	1.25	1.21	1.22
3	115.85	1.19	1.65	1.62	1.52	1.48

According to Table 3 and Figure 5, the solution convergence at Re = 1.16 is obtained in $t^* = 0.6$. The PDF of the normalised x-direction velocity in Figure 5-(a) can be divided into (i) the negative velocities, (ii) the positive velocities lower than 1.0, and (iii) the positive velocities higher than 1.0, similar to the results in Figure 2-(a) for the SC-packed porous medium. The separation of the positive normalised x-direction velocities at 1.0 confirms the presence of two different flow signatures. This separation, however, is not as clear as that of the SC-packed porous medium. It should be noted that the presence of the negative x-direction velocities here would not be necessarily due to the recirculating flows, simply because it is likely to have the flow pathways opposite to the imposed flow direction hence the backflow may occur [42,43]. Apart from that, the trajectory of the main flow pathways essentially depends on the arrangement of the solid particles; therefore, the recirculating flows in directions other than the imposed flow direction may exist in a tortuous porous medium, enhancing the transport between the main flow pathways and the stagnant zones. The tortuosity of the randomly-packed porous structure is 1.2 (see [60]), close to that of the SC-packed structure (i.e. 1.0), implying the main flow pathways must be still aligned with the x-direction. Since almost 0.1% of the x-direction velocity data are negative, it can be elucidated that there is almost no streamwise flow recirculation and the Stokes flow is dominant throughout the domain at such a low Re. The evolution of the PDFs of the normalised velocities in the y- and z- directions are provided in Figure 5-(b) and (c), respectively. As expected, the distributions are no longer symmetric essentially due to the geometrical asymmetry of the domain, and two different functions are required to characterise the velocity in both directions.

The velocity PDFs in Figure 5-(d) exhibit two different signatures, and the distinction point is 1.05. The velocities higher than this distinction point are required to be characterised with an exponential PDF model (see log-linear PDF plot) whereas a power-law model describes the PDF of the lower velocities (see log-log PDF plot).

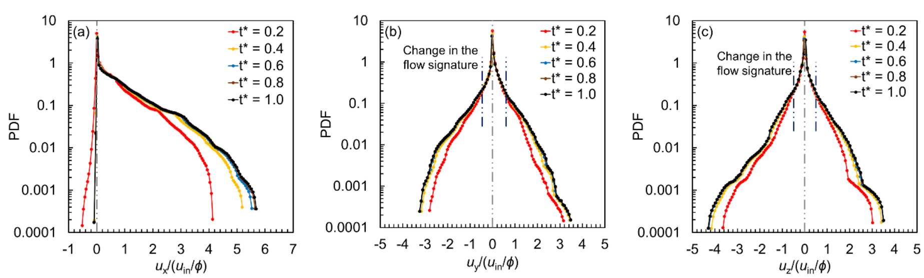

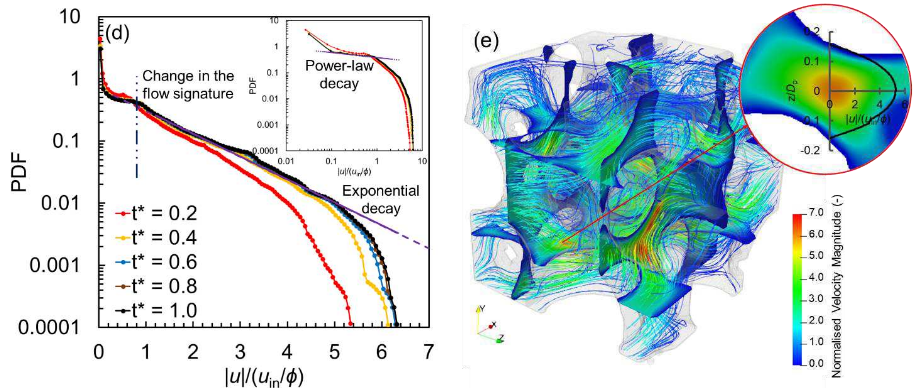

Figure 5. Temporal evolution of the normalised velocity fields within the randomly-packed porous structure at Re = 1.16: (a-d) log-linear PDF plot of the normalised velocity magnitude and its components in the x, y, and z-directions, and (e) the spatial distribution and streamlines of the velocity field at $t^* = 1.0$. The inset in (d) is the log-log plot of the PDF of the normalised velocity magnitude.

The evolutions of the PDFs of the normalised velocity magnitude and its components at Re = 11.59 are illustrated in Figure 6. According to Table 3, the solution convergence is obtained in $t^* = 0.6$, and the trends of the PDFs are generally similar to those at Re = 1.16. However, a higher number of the negative x-direction velocity data (~0.9% of the velocity data) is observed in Figure 6-(a) compared to those in Figure 5-(a), implying the formation of the recirculating flows at the stagnant zones. However, these flow structures are not numerous and large enough to influence the flow field; therefore, no delay in the solution convergence is observed. This fact can also be confirmed by investigating the separation point of the flow signatures in Figure 6-(d). As observed, the separation point is 0.82, lower than that of the previous case, suggesting limited low-velocity zones, in which the flow is likely to become recirculated, and wider high-velocity regions, where the flow can be characterised with an exponential PDF model.

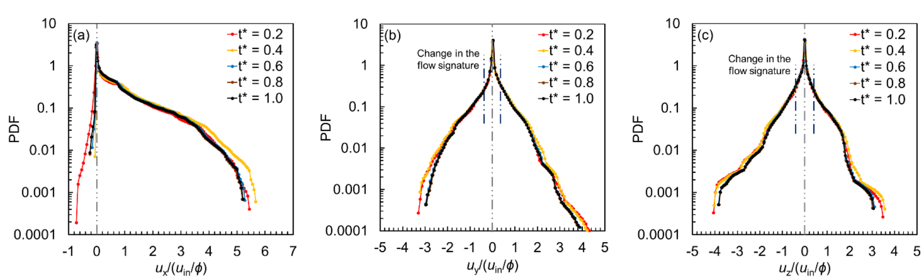

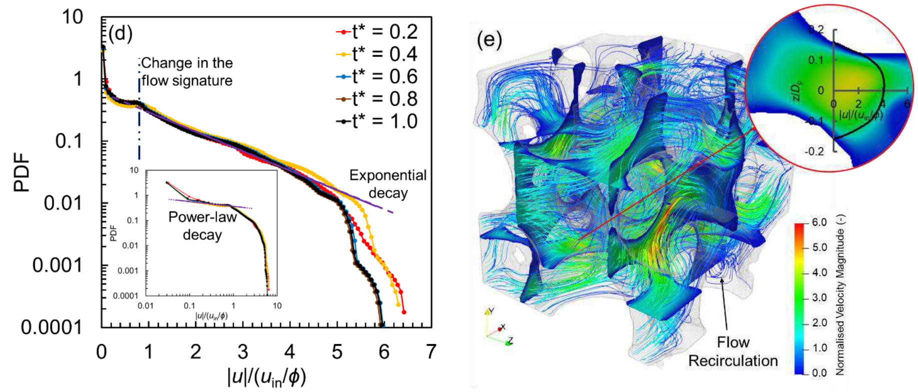

Figure 6. Temporal evolution of the normalised velocity fields within the randomly-packed porous structure at Re = 11.59: (a-d) log-linear PDF plot of the normalised velocity magnitude and its components in the x, y, and z-directions, and (e) the spatial distribution and streamlines of the velocity field at $t^* = 1.0$. The inset in (d) is the log-log plot of the PDF of the normalised velocity magnitude.

The PDF of the velocity magnitude and its components at Re = 115.85 is illustrated in Figure 7. As evidenced by the average velocities presented in Table 3, the solution convergence is obtained in $t^* = 0.8$, and the flow becomes fully developed in many regions. However, there are still discrepancies in the PDF of the normalised velocity magnitude and its x-direction component at the values higher than 3.6, covering almost 3.0% of the velocity data. These discrepancies can be related to the instability of the flow at the converging/diverging pore throats and the large-scale high-velocity vortical structures in the main flow pathways (see Figure 7-(e)).

The PDF of the normalised x-direction velocities is shown in Figure 7-(a). The separation of the positive normalised velocities at 0.8 confirms the presence of two distinctive flow signatures (which will be discussed later). The negative velocities are almost 13% of the velocity data, significantly higher than those in the lower Re. Moreover, in contrast to the PDF of the velocities shown in Figure 5 and Figure 6 at lower Re, the discrepancies are observed in the tail of the PDF at both negative and positive x-direction velocities after the convergence of the solution, a behaviour that can be also seen in the PDF of the normalised velocities in the y- and z-directions (Figure 7-(b) and (c)). Such discrepancies essentially cannot be caused by the flow recirculation (which would be expected to form in the stagnant zones), and they are due to the presence of the high-velocity vortical structures in the main flow pathways, confirming the dominance of the turbulent flow regime.

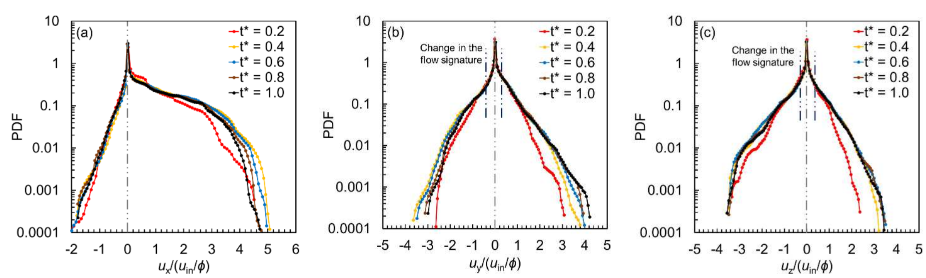

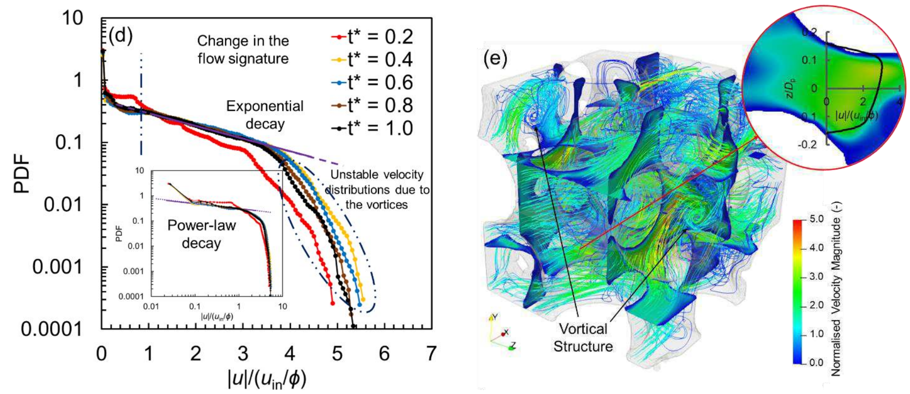

Figure 7. Temporal evolution of the normalised velocity fields within the randomly-packed porous structure at Re = 115.85: (a-d) log-linear PDF plot of the normalised velocity magnitude and its components in the x, y, and z-directions, and (e) the spatial distribution and streamlines of the velocity field at $t^* = 1.0$. The inset in (d) is the log-log plot of the PDF of the normalised velocity magnitude.

The log-linear PDF plot of the normalised velocity magnitude in Figure 7-(d) is fairly similar to that of the x-direction velocity, as expected, and an exponential function can be used to characterise the velocity distribution, in contrast to what observed for the SC-packed structure in Figure 4-(d). The underlying reason for such a different flow signature is that the main flow pathways in the SC-packed medium are all aligned with the imposed flow direction. Thus, the velocity profile of the fluid jet entering this non-tortuous structure would not be disturbed significantly by the solid boundaries. Consequently, the flow keeps its turbulent (non-parabolic) characteristics when flowing in the main pathways, a Laplace function can be used to characterise the flow in these regions, and obvious boundaries would be created between the low- and high-velocity zones, all perpendicular to the imposed flow direction. On the other hand, when the fluid flows in the randomly-packed medium with a higher tortuosity (i.e. more disturbances from the solid boundaries), the flow cannot keep its non-parabolic characteristics and its velocity profile becomes influenced by the no-slip boundary conditions hence an exponential decay is observed in the PDF of the velocities, similar to the results for lower Re.

As discussed above, the distribution of the velocity magnitude and its components in the randomly-packed porous medium must be quantified with two functions at various Re. The type and parameter(s) of the PDF models fitted to the distribution of the normalised velocity magnitudes at both low- and high-velocity zones are summarised in Table 4. In the low-velocity regions, it is observed that k still does not show a clear and strong sensitivity to Re whereas comparing its values to those reported in Table 2 reveals its dependence on the pore structure, suggesting the evolution of the distribution of the velocity magnitude from power-law toward flat and uniform behaviour when the heterogeneity increases. It should be noted that the flat distribution of the velocity in the low-velocity zones has been observed in the other studies [43,74]. In the high-velocity regions, λ shows an inverse proportionality to Re, in contrast to the observations in Table 2. Such a contradiction suggests that λ must be sensitive to both Re and the tortuosity of the porous structure.

Table 4. Summary of the type and parameter(s) of the models fitted to the PDF of the velocity magnitudes in the randomly-packed porous structure. u^* here the normalised velocity magnitude, $|u|/(u_{in}/\phi)$.

No.	Re	PDF model

		Low-velocity zones	High-velocity zones	Distinctive normalised velocity magnitude (-)
1	1.16	$PDF \propto u^{*-k}, k = 0.218$	$PDF \propto e^{-\lambda u^*}, \lambda = 0.835$	1.00
2	11.59	$PDF \propto u^{*-k}, k = 0.291$	$PDF \propto e^{-\lambda u^*}, \lambda = 0.773$	0.82
3	115.85	$PDF \propto u^{*-k}, k = 0.316$	$PDF \propto e^{-\lambda u^*}, \lambda = 0.507$	0.80

As discussed above, the negative x-direction velocities can be directly correlated to the flow recirculation. Thus, the effect of the pore space heterogeneity on the formation of the recirculating flow structures can be understood by comparing the distribution of the negative x-direction velocities of the randomly-packed structure with that of the SC-packed medium. Referring to the PDF of the velocities, the fractions of the negative x-direction velocities in the SC-packed porous structure are markedly higher than those in the randomly-packed structure. This evidently demonstrates that it is more likely to observe the flow recirculation in the wake of grain particles in the orderly-packed structures, where the trajectory of the main flow pathways is less distorted, and there are clear boundary surfaces between the low-velocity stagnant zones and the high-velocity main pathways; this will be discussed further in Section 3.2.

3.2 Analysis of the flow in the low-velocity regions

In Section 3, the analysis of the PDF of the velocity magnitude and its components in both porous structures at different Re confirmed that two different PDF models should be employed to characterise the flow field in porous media, regardless of the packing and heterogeneity of the porous structure. Referring to the velocity PDF data at different Re indicates that at least more than 65% and 45% of the velocity magnitudes in the SC- and randomly-packed structures are lower than the distinction point of the flow signatures, respectively. We provide further insights into the features of the velocity distribution at the low-velocity regions because it essentially controls the longitudinal dispersion of the scalar parameters being transported in porous media [75–77]. The PDF of the converged normalised velocity magnitudes, sampled uniformly in bins of their logarithm, for both SC- and randomly-packed porous structures are provided in Figure 8, on semi- and doubly-logarithmic axes. As observed, the flow signatures at lower velocities are quite similar to each other, exhibiting a tube-like behaviour, see [59], which is expected since both porous structures are not heterogeneous. Besides, the characteristics of the flow in the two lower Re, where the flow regime is laminar, are closer to each other at the high normalised velocities, compared to the trend observed for the highest Re, where the flow becomes turbulent. In particular, it can be seen that the change of the flow behaviour from laminar to turbulent regime results in the spread of the high-velocity peak becoming narrower, taller, and occurring at a higher normalised velocity.

The insights into the effect of the pore structure on the flow behaviour can be obtained via investigating the trend and the range of the velocity PDFs. As observed in Figure 8-(a), the PDF of the normalised velocity in the SC-packed medium exhibits a bimodal behaviour, and the variations of the velocities are almost six orders of magnitude (10^{-5} – 10^{1}), regardless of Re. The bimodal trend of the velocity PDF is expected because there are clear and connected boundary surfaces between the low-velocity stagnant zones and the high-velocity main pathways; these boundaries have been observed in the other experimental and modelling works studying transport in the homogeneous ordered porous structures [72,78,79].

It is also observed that the first peak, representing the recirculating flow structures, becomes taller and shifts toward higher normalised velocity values when Re increases. This behaviour supports our discussion regarding the effect of Re on the size of the recirculating flows and their velocities presented in Section 3.1.1.

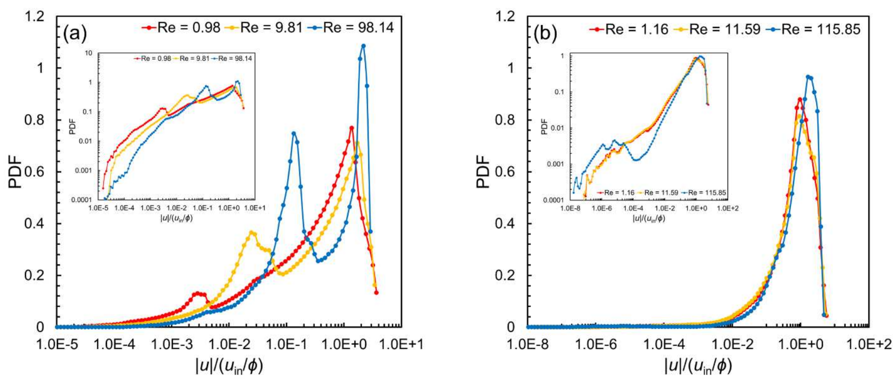

Figure 8. Probability density function (PDF) of the converged velocity magnitudes for the (a) SC-packed and (b) randomly-packed porous structures on semi-logarithmic axes. The inset in each plot is the same PDF on doubly logarithmic axes.

In Figure 8-(b), a unimodal trend is observed for the PDF of the velocity in the randomly-packed medium at different Re and the variations of the velocities are almost nine orders of magnitude (10^{-8} – 10^{1}). The unimodal trend of the velocity PDF indicates the random arrangement of the solid particles has caused the formation of a limited number of recirculating flow structures. Comparing the trend and wider variations of the velocity PDF in the randomly-packed medium to that of the SC-packed medium confirms that the tortuosity, even being small, plays a key role in controlling the spatial distribution and size of the low- and high-velocity regions as well as the possibility of formation of different flow structures in the pore space. Such distinctive characteristics are essential to be considered when studying the transport of the scalar phenomena in porous media as they are inherently influenced by the flow signature.

3.3 Tortuosity and local Re: The key parameters to understanding different flow signatures in porous media

The analysis of the PDFs in the previous sections indicates that the flow characteristics in a given porous medium depend upon the competition of the viscous and inertial driving forces as well as the geometry of the pore structure. Therefore, the type and extent of the flow signatures can be correlated to the tortuosity and flow rate. In this section, according to the insights obtained in the previous sections into the effect of the flow regime and pore structure on the flow behaviour, we propose a general framework for determination of the most possible flow signatures and their velocity PDFs in a packed-bed porous structure with respect to its tortuosity and local Re.

Figure 9 illustrates the colour map of the PDFs versus the tortuosity and local Re. As evidenced by our discussion in the previous sections, the flow in porous media can be described with three possible velocity PDFs:

i. Power-law PDF: Regardless of the tortuosity, the power-law PDF is most likely to be found in the vicinity of the solid boundaries and the stagnant regions (such as dead-end pores or the wake of the solid particles), where the local Re is small and the flow is highly influenced by the solid-fluid interface. In addition, analysis of the distinction points at which the PDF of the velocity changes from the power-law (to either exponential or Laplace) shows that increasing the tortuosity results in shrinkage of the range of the power-law PDF dominance. It should be noted that investigations on the flow characteristics in highly-tortuous and heterogeneous structures are required to provide reliable insights into high-tortuosity conditions.

ii. Exponential PDF: The exponential PDF can be found in the main pathways where the fluid flows with a higher velocity and the effect of the inertia is not negligible. The prevalence of this flow signature in an individual pore highly depends on the extent the viscous forces can be transmitted from the solid-fluid interface toward the pore centre and shape the velocity profile. Therefore, the exponential PDF would be expected to be seen in the main pathways of tortuous porous media at moderate and high local Re while at non-tortuous media, it is likely to be found only at moderate local Re.

iii. Laplace PDF: This PDF can only be seen in the main pathways of non-tortuous porous media at the high local Re where there is almost no solid obstacle in front of the flow and the velocity profile is non-parabolic.

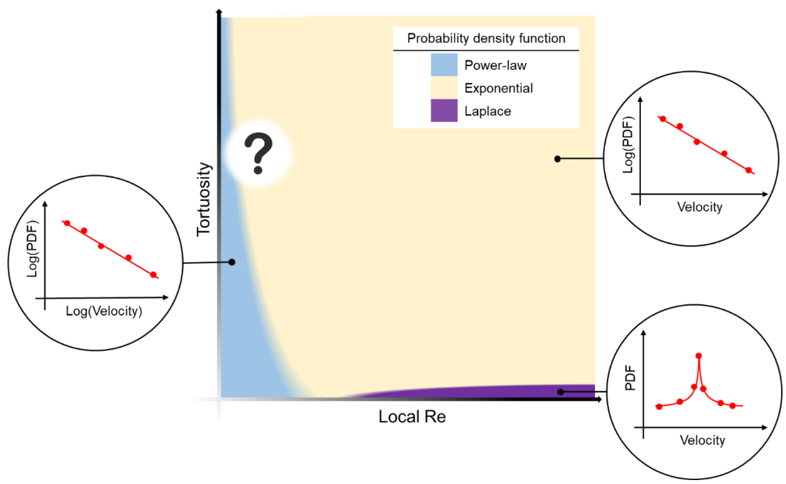

Figure 9. Proposed colour map of the PDFs of the velocity fields as a function of the tortuosity and local Re.

It should be noted that the above framework is qualitative and created based on the analysis of the velocity PDFs in backed-bed structures; therefore, its application in its current form might only be limited to the fields concerned with packed-bed porous media. We believe more modelling and experimental studies with a focus on the other potential key factor such as porosity, surface roughness, and particle size distribution assist with obtaining a better understanding of the flow dependency on the properties of the host medium. The fruits of these future studies are essential to be used for quantifying the proposed framework. Geostatistical analysis of the velocity data can also help with establishing a robust correlation between the microscale flow details and the macroscale effective properties such as permeability in different regimes.

4. Conclusions

In this work, we conducted single-phase fluid flow simulation using LBM to shed light on the pore-scale flow characteristics in 3D SC- and randomly-packed porous structures. The ultra-fine mesh size considered in the simulations made it possible to carry out the simulations at three orders of magnitude of Re, covering laminar to turbulent flow regimes, and capture different flow signatures. The following conclusions can be drawn from this study:

i. Regardless of the pore structure, the pore velocity fields in porous media at different Re cannot be characterised with a single PDF because the flow signature at the main pathways, where the velocity magnitudes are higher hence most of the fluid transport is carried, is different from that of the low-velocity regions such as the wake of the solid particles and the vicinity of the solid boundaries, where the velocity is lower. These flow signatures exhibit their own specific behaviour in the PDF plot of the velocity magnitude, and there is always a distinction point, at which the velocity PDFs meet.
ii. The velocities lower than the distinction point can be characterised by a power-law PDF model for both SC- and randomly-packed porous media. The velocities higher than the distinctive value, however, should be described with a different PDF model. The analysis of the PDFs of the velocities suggests the exponential model when Re is low and the flow is laminar. When Re is high and the flow is turbulent, the velocity exhibits a Laplace PDF for the SC-packed medium with the tortuosity of 1.0, owing to the fact that the main flow pathways are all aligned with the imposed flow direction. For the randomly-packed medium with the tortuosity of 1.2, however, the flow signature is quite similar to that of lower Re hence could be characterised by an exponential PDF model.
iii. As expected, the PDF of the positive x-direction velocities have the same characteristics as those of the velocity magnitudes. The presence of the negative x-direction velocities can be due to recirculating flows oriented in the flow direction, vortical structures, or simply backflow. It was observed that the negative velocities are created due to the flow recirculation at the stagnant regions for the non-tortuous SC-packed medium while they are caused by the backflow at low Re and vortical structures at highest Re.
iv. Analysis of the velocity data in y- and z- directions shows that the velocity components perpendicular to the imposed flow direction should be also characterised by two different PDFs, and there is a distinctive point in these directions too.
v. Analysis of the flow in the low-velocity zones shows that the distribution of the velocities in these regions as well as the boundary between the low- and high-velocities highly depends on the arrangement of the solid particles and tortuosity of the porous structure. For the SC-packed medium, the regular arrangement of the solid particles causes a clear and connected boundary to form between these two flow signatures. Such a clear boundary, however, does not exist for the randomly-packed tortuous medium.

5. Supplementary Material

The PDFs of the velocities (magnitude as well as components) for both SC- and randomly-packed porous media can be found in Supplementary Material. All the figures reported in Section 3 have been extracted by referring to and analysing these PDF data.

6. Acknowledgement

The authors gratefully acknowledge support from the Warwick EPSRC Impact Acceleration Fund (EP/R511808/1).

7. Appendix A: Validation of the code

Fluid flow through a cylindrical tube driven by a pressure gradient known as Poiseuille flow is extensively used as a benchmark to verify the accuracy and convergence of various CFD methods [51,52]. The exact analytical solution for Poiseuille flow in a cylindrical coordinate can be expressed as [80]:

$$u_x(r) = \frac{1}{4\nu}\left(-\frac{\partial p}{\partial x}\right)(R^2 - r^2) \tag{A1}$$

where $u_x(r)$ is the axial velocity, $\frac{\partial p}{\partial x}$ is the pressure gradient, R is the radius of the cylindrical tube, and r is the distance from the centreline of the tube.

We validated the developed code by simulating Poiseuille flow in a cylindrical tube (having the diameter of 100 μm and resolution of 1 μm per lattice length) and comparing the velocity profile along the diameter of the tube against that of the analytical solution. The results are presented in Figure A1, showing that the normalised velocities in the x-direction obtained from the numerical solution agree perfectly with the exact analytical solution.

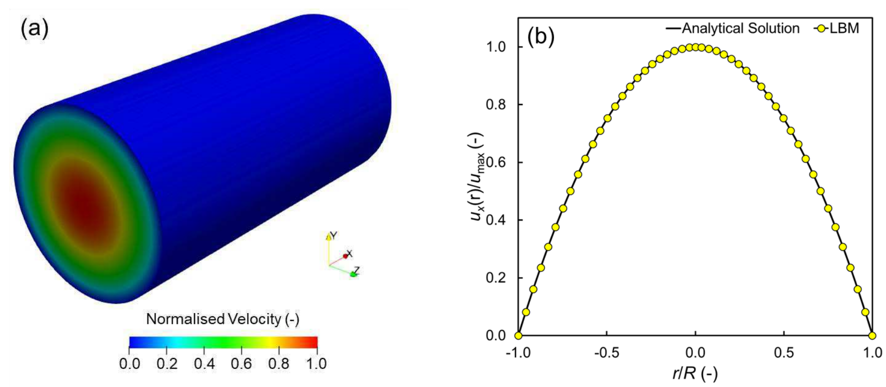

Figure A1. Poiseuille flow through a cylindrical tube: (a) normalised velocity field obtained via the numerical simulation, and (b) comparison between the velocity profiles along the diameter of the tube obtained via the numerical simulation and the exact analytical solution.

8. References

[1] G. Zhu, J. Yao, A. Li, H. Sun, and L. Zhang, Energy Fuels **31**, 5324 (2017).
[2] A. Xu, W. Shyy, and T. Zhao, Acta Mech. Sin. **33**, 555 (2017).
[3] S. Bakhshian, H.S. Rabbani, S.A. Hosseini, and N. Shokri, Geophysical Research Letters **47**, e2020GL088187 (2020).
[4] A. Jahanbakhsh, O. Shahrokhi, and M.M. Maroto-Valer, Sci Rep **11**, 17847 (2021).
[5] H. Moghimi, M. Siavashi, M. Mousavi Nezhad, and A. Guadagnini, Sustainable Energy Technologies and Assessments **52**, 102048 (2022).
[6] E.M. Ekanem, S. Berg, S. De, A. Fadili, T. Bultreys, M. Rücker, J. Southwick, J. Crawshaw, and P.F. Luckham, Phys. Rev. E **101**, 042605 (2020).
[7] S.S. Datta, H. Chiang, T.S. Ramakrishnan, and D.A. Weitz, Phys. Rev. Lett. **111**, 064501 (2013).
[8] A.A. El-Zehairy, M.M. Nezhad, V. Joekar-Niasar, I. Guymer, N. Kourra, and M.A. Williams, Advances in Water Resources **131**, 103378 (2019).
[9] M. Mousavi Nezhad, M. Rezania, and E. Baioni, Transp Porous Med **126**, 5 (2019).
[10] C.T. DeGroot and A.G. Straatman, Journal of Heat Transfer **134**, (2012).
[11] F.A. Khan and A.G. Straatman, International Journal of Heat and Mass Transfer **101**, 1003 (2016).
[12] R. Aziz, V. Joekar-Niasar, and P. Martinez-Ferrer, International Journal of Multiphase Flow **109**, 51 (2018).
[13] T. Nguyen, R. Muyshondt, Y.A. Hassan, and N.K. Anand, Physics of Fluids **31**, 025101 (2019).
[14] S. Yoon and P.K. Kang, Phys. Rev. Fluids **6**, 014502 (2021).

[15] M.J. Blunt, B. Bijeljic, H. Dong, O. Gharbi, S. Iglauer, P. Mostaghimi, A. Paluszny, and C. Pentland, Advances in Water Resources **51**, 197 (2013).
[16] S. Bakhshian, S.A. Hosseini, and N. Shokri, Sci Rep **9**, 3377 (2019).
[17] A. Banerjee, S. Pasupuleti, K. Mondal, and M.M. Nezhad, International Journal of Heat and Mass Transfer **179**, 121650 (2021).
[18] N.F. Jouybari, M. Maerefat, and M.E. Nimvari, Heat Mass Transfer **52**, 269 (2016).
[19] Y. Jin and A.V. Kuznetsov, Physics of Fluids **29**, 045102 (2017).
[20] B.D. Wood, X. He, and S.V. Apte, Annual Review of Fluid Mechanics **52**, 171 (2020).
[21] T. Nguyen, S. King, and Y. Hassan, Exp Fluids **62**, 72 (2021).
[22] K. Singh, H. Menke, M. Andrew, C. Rau, B. Bijeljic, and M.J. Blunt, Sci Data **5**, 180265 (2018).
[23] B. Wei, X. Zhang, R. Wu, P. Zou, K. Gao, X. Xu, W. Pu, and C. Wood, Fuel **246**, 34 (2019).
[24] Y.A. Hassan and E.E. Dominguez-Ontiveros, Nuclear Engineering and Design **238**, 3080 (2008).
[25] S. Khayamyan, T.S. Lundström, P. Gren, H. Lycksam, and J.G.I. Hellström, Transp Porous Med **117**, 45 (2017).
[26] I.A.S. Larsson, T.S. Lundström, and H. Lycksam, Exp Fluids **59**, 96 (2018).
[27] T. Bultreys, K. Singh, A.Q. Raeini, L.C. Ruspini, P.-E. Øren, S. Berg, M. Rücker, B. Bijeljic, and M.J. Blunt, Water Resources Research **56**, e2019WR026587 (2020).
[28] T. Pak, L.F. de L. Luz, T. Tosco, G.S.R. Costa, P.R.R. Rosa, and N.L. Archilha, Proceedings of the National Academy of Sciences **117**, 13366 (2020).
[29] X. Yang, Y. Mehmani, W.A. Perkins, A. Pasquali, M. Schönherr, K. Kim, M. Perego, M.L. Parks, N. Trask, M.T. Balhoff, M.C. Richmond, M. Geier, M. Krafczyk, L.-S. Luo, A.M. Tartakovsky, and T.D. Scheibe, Advances in Water Resources **95**, 176 (2016).
[30] A. Golparvar, Y. Zhou, K. Wu, J. Ma, and Z. Yu, Advances in Geo-Energy Research **2**, 418 (2018).
[31] Q. Xiong, T.G. Baychev, and A.P. Jivkov, Journal of Contaminant Hydrology **192**, 101 (2016).
[32] D.(孔德彬) Kong, P.(廉培庆) Lian, W.(朱维耀) Zhu, and Y.(李宜强) Li, Physics of Fluids **32**, 122004 (2020).
[33] B.(韦贝) Wei, J.(侯健) Hou, M.C. Sukop, and Q.(杜庆军) Du, Physics of Fluids **32**, 092105 (2020).
[34] J. Tian, C. Qi, Y. Sun, Z.M. Yaseen, and B.T. Pham, Engineering with Computers **37**, 3455 (2021).
[35] T. Krüger, H. Kusumaatmaja, A. Kuzmin, O. Shardt, G. Silva, and E.M. Viggen, Springer International Publishing **10**, 4 (2017).
[36] Z.-Q. Dong, L.-P. Wang, C. Peng, and T. Chen, Physics of Fluids **34**, 093608 (2022).
[37] E. Baioni, M. Mousavi Nezhad, G.M. Porta, and A. Guadagnini, Physics of Fluids **33**, 106604 (2021).
[38] C. Pan, L.-S. Luo, and C.T. Miller, Computers & Fluids **35**, 898 (2006).
[39] A. Eshghinejadfard, L. Daróczy, G. Janiga, and D. Thévenin, International Journal of Heat and Fluid Flow **62**, 93 (2016).
[40] M. Vasheghani Farahani, A. Hassanpouryouzband, J. Yang, and B. Tohidi, Water Resources Research **56**, e2020WR027885 (2020).
[41] M. Matyka, J. Gołembiewski, and Z. Koza, Phys. Rev. E **93**, 013110 (2016).
[42] M. Dentz, M. Icardi, and J.J. Hidalgo, Journal of Fluid Mechanics **841**, 851 (2018).
[43] M. Souzy, H. Lhuissier, Y. Méheust, T. Le Borgne, and B. Metzger, Journal of Fluid Mechanics **891**, (2020).

[44] V.L. Morales, M. Dentz, M. Willmann, and M. Holzner, Geophysical Research Letters **44**, 9361 (2017).
[45] M. Carrel, V.L. Morales, M. Dentz, N. Derlon, E. Morgenroth, and M. Holzner, Water Resources Research **54**, 2183 (2018).
[46] M.S.K.F.S. AlAdwani, Prediction of Velocity Distribution from the Statistics of Pore Structure in 3D Porous Media via High-Fidelity Pore-Scale Simulation, Thesis, Massachusetts Institute of Technology, 2017.
[47] P.K. Kang, P. de Anna, J.P. Nunes, B. Bijeljic, M.J. Blunt, and R. Juanes, Geophysical Research Letters **41**, 6184 (2014).
[48] M. Holzner, V.L. Morales, M. Willmann, and M. Dentz, Phys. Rev. E **92**, 013015 (2015).
[49] M. Piller, D. Casagrande, G. Schena, and M. Santini, J. Phys.: Conf. Ser. **501**, 012010 (2014).
[50] R.F. Mardanov, S.K. Zaripov, and D.V. Maklakov, Engineering Analysis with Boundary Elements **113**, 204 (2020).
[51] R. Soleimani, M. Zargartalebi, J. Azaiez, and I.D. Gates, Physics of Fluids **33**, 012011 (2021).
[52] M. Vasheghani Farahani, S. Foroughi, S. Norouzi, and S. Jamshidi, Journal of Energy Resources Technology **141**, (2019).
[53] A. De Rosis and C. Coreixas, Physics of Fluids **32**, 117101 (2020).
[54] M. Jiang, Z.G. Xu, and Z.P. Zhou, Journal of Petroleum Science and Engineering **204**, 108712 (2021).
[55] M.J. Krause, A. Kummerländer, S.J. Avis, H. Kusumaatmaja, D. Dapelo, F. Klemens, M. Gaedtke, N. Hafen, A. Mink, R. Trunk, J.E. Marquardt, M.-L. Maier, M. Haussmann, and S. Simonis, Computers & Mathematics with Applications **81**, 258 (2021).
[56] J. Ahrens, B. Geveci, and C. Law, The Visualization Handbook **717**, (2005).
[57] M. Prodanović and S.L. Bryant, Journal of Colloid and Interface Science **304**, 442 (2006).
[58] J.L. Finney and J.D. Bernal, Proceedings of the Royal Society of London. A. Mathematical and Physical Sciences **319**, 479 (1970).
[59] B. Bijeljic, A. Raeini, P. Mostaghimi, and M.J. Blunt, Phys. Rev. E **87**, 013011 (2013).
[60] B.P. Muljadi, M.J. Blunt, A.Q. Raeini, and B. Bijeljic, Advances in Water Resources **95**, 329 (2016).
[61] N.J. Dyck and A.G. Straatman, International Journal of Heat and Mass Transfer **81**, 470 (2015).
[62] C. Coreixas, G. Wissocq, B. Chopard, and J. Latt, Philosophical Transactions of the Royal Society A: Mathematical, Physical and Engineering Sciences **378**, 20190397 (2020).
[63] P.K. Kundu, I.M. Cohen, and D.R. Dowling, in *Fluid Mechanics (Sixth Edition)*, edited by P.K. Kundu, I.M. Cohen, and D.R. Dowling (Academic Press, Boston, 2016), pp. 469–532.
[64] R.J. Hill, D.L. Koch, and A.J.C. Ladd, Journal of Fluid Mechanics **448**, 243 (2001).
[65] J.S. Andrade, M.P. Almeida, J. Mendes Filho, S. Havlin, B. Suki, and H.E. Stanley, Phys. Rev. Lett. **79**, 3901 (1997).
[66] R.J. Hill, D.L. Koch, and A.J.C. Ladd, J. Fluid Mech. **448**, 213 (2001).
[67] M. Siena, M. Riva, J.D. Hyman, C.L. Winter, and A. Guadagnini, Phys. Rev. E **89**, 013018 (2014).
[68] B. Bijeljic, A.Q. Raeini, Q. Lin, and M.J. Blunt, (2018).
[69] M. Mousavi Nezhad and A.A. Javadi, Journal of Hazardous, Toxic, and Radioactive Waste **15**, 208 (2011).
[70] C. Iwaki, K.H. Cheong, H. Monji, and G. Matsui, Exp Fluids **37**, 350 (2004).
[71] S.S. Paul, M.F. Tachie, and S.J. Ormiston, International Journal of Heat and Fluid Flow **28**, 441 (2007).

[72] M. Delgado, S. Lee, Y.A. Hassan, and N.K. Anand, International Journal of Heat and Mass Transfer **122**, 614 (2018).
[73] J. Štigler, Engineering Mechanics **21**, 371 (2014).
[74] P. de Anna, B. Quaife, G. Biros, and R. Juanes, Phys. Rev. Fluids **2**, 124103 (2017).
[75] B. Berkowitz and H. Scher, Water Resources Research **31**, 1461 (1995).
[76] B. Bijeljic, P. Mostaghimi, and M.J. Blunt, Phys. Rev. Lett. **107**, 204502 (2011).
[77] Y.(陈奕林) Chen, G.(金光球) Jin, P.(张沛) Zhang, Q.(姜启豪) Jiang, S.(吴思麟) Wu, S.A. Galindo Torres, and L.(李凌) Li, Physics of Fluids **33**, 126601 (2021).
[78] V. Srikanth, C.-W. Huang, T.S. Su, and A.V. Kuznetsov, Journal of Fluid Mechanics **929**, A2 (2021).
[79] S. Lee and Y.A. Hassan, International Journal of Heat and Fluid Flow **95**, 108950 (2022).
[80] S. Kumar, in *Fluid Mechanics (Vol. 2): Basic Concepts and Principles*, edited by S. Kumar (Springer International Publishing, Cham, 2023), pp. 181–282.

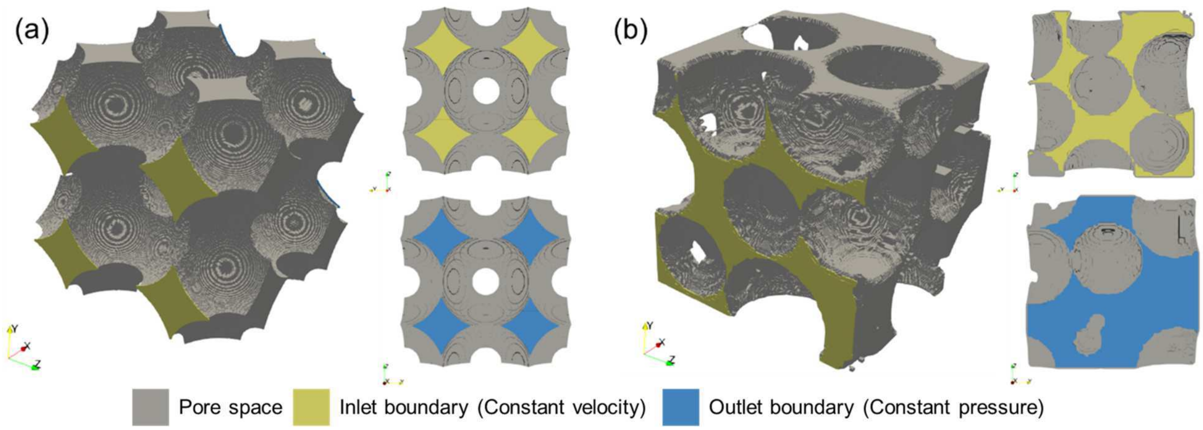
(a)
(b)
Pore space
Inlet boundary (Constant velocity)
Outlet boundary (Constant pressure)

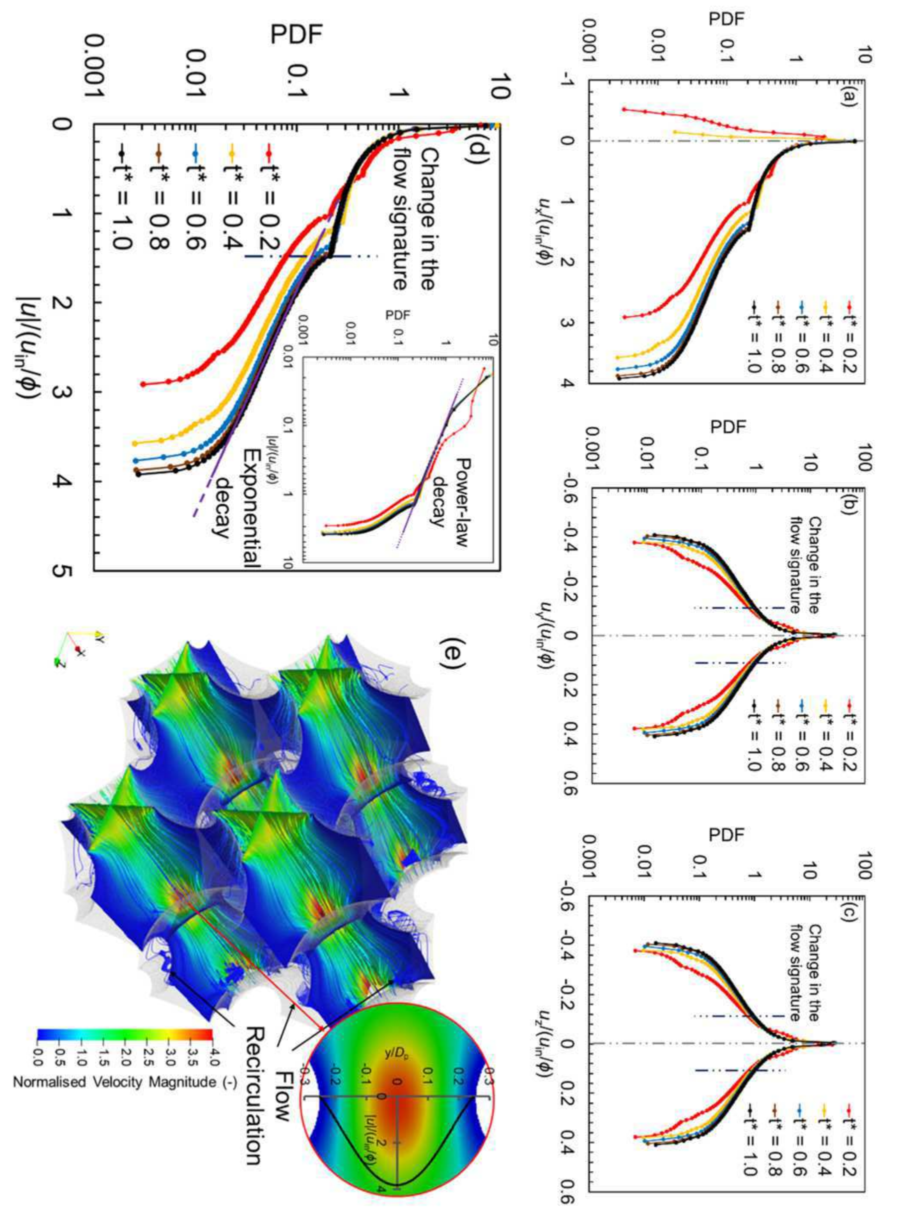
(a)
(b)
(c)
(d)
(e)
PDF
$u_x/(u_{in}/\phi)$
$u_y/(u_{in}/\phi)$
$u_z/(u_{in}/\phi)$
$|u|/(u_{in}/\phi)$
t* = 0.2
t* = 0.4
t* = 0.6
t* = 0.8
t* = 1.0
Change in the flow signature
Power-law decay
Exponential decay
Flow Recirculation
Normalised Velocity Magnitude (-)
y/D_p

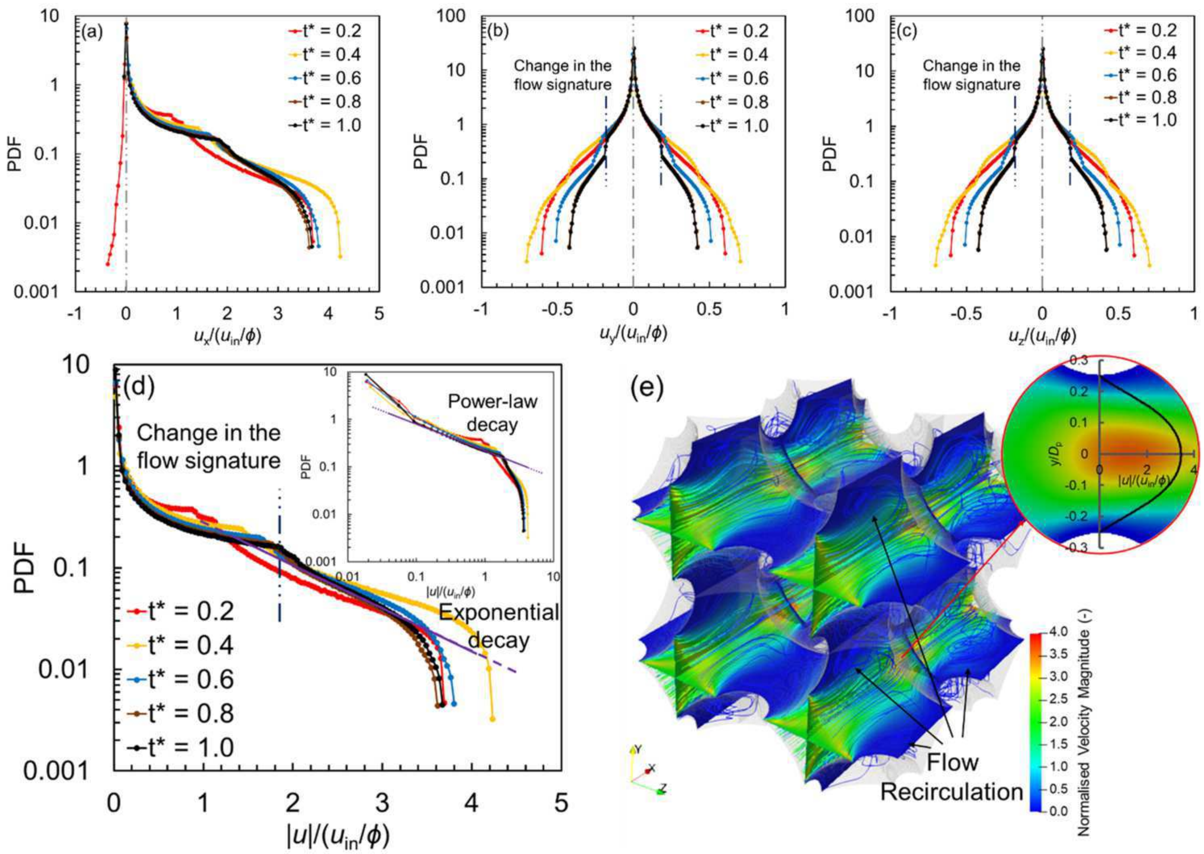
(a)
(b)
(c)
(d)
(e)
t* = 0.2
t* = 0.4
t* = 0.6
t* = 0.8
t* = 1.0
PDF
$u_x/(u_{in}/\phi)$
$u_y/(u_{in}/\phi)$
$u_z/(u_{in}/\phi)$
$|u|/(u_{in}/\phi)$
Change in the flow signature
Power-law decay
Exponential decay
Flow Recirculation
Normalised Velocity Magnitude (-)
y/D_p

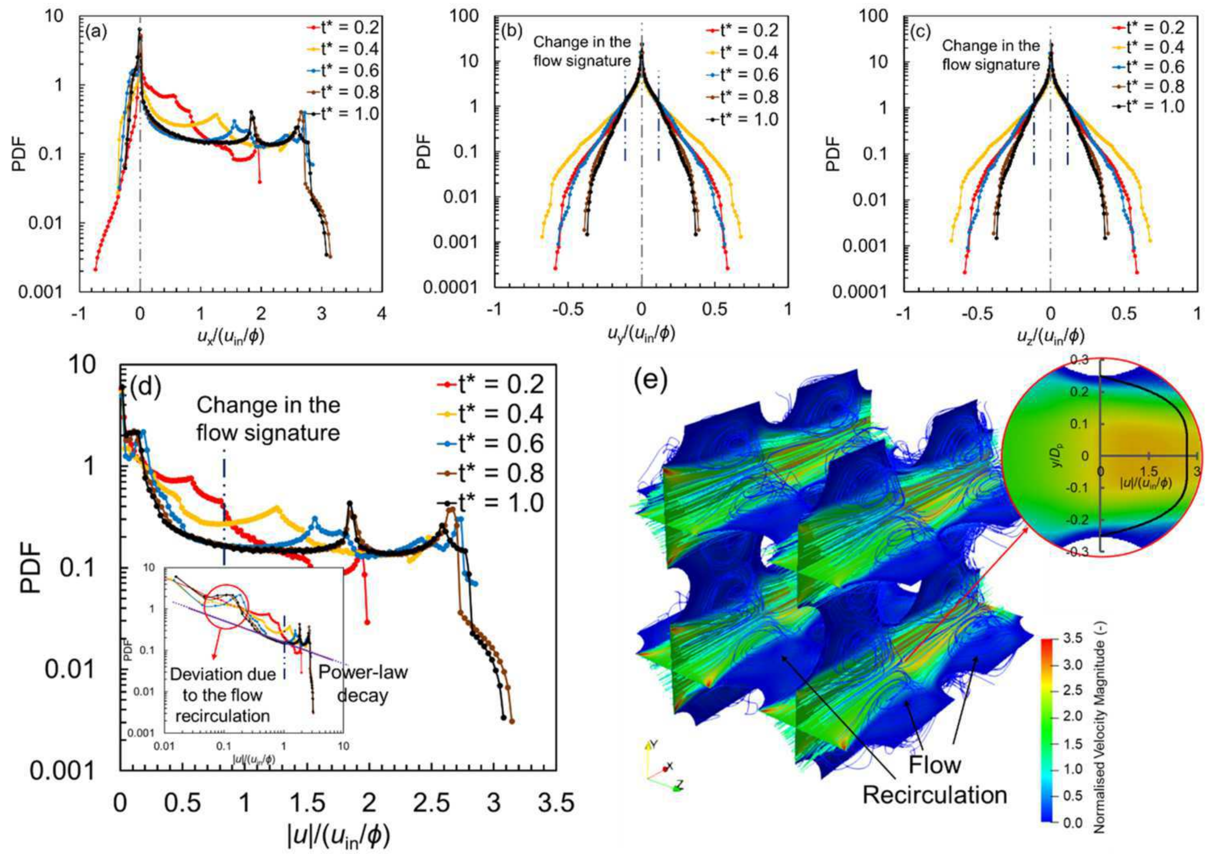
(a)
PDF
$u_x/(u_{in}/\phi)$
t* = 0.2
t* = 0.4
t* = 0.6
t* = 0.8
t* = 1.0
(b)
Change in the flow signature
$u_y/(u_{in}/\phi)$
(c)
Change in the flow signature
$u_z/(u_{in}/\phi)$
(d)
Change in the flow signature
$|u|/(u_{in}/\phi)$
Deviation due to the flow recirculation
Power-law decay
(e)
y/D_p
$|u|/(u_{in}/\phi)$
Normalised Velocity Magnitude (-)
Flow Recirculation

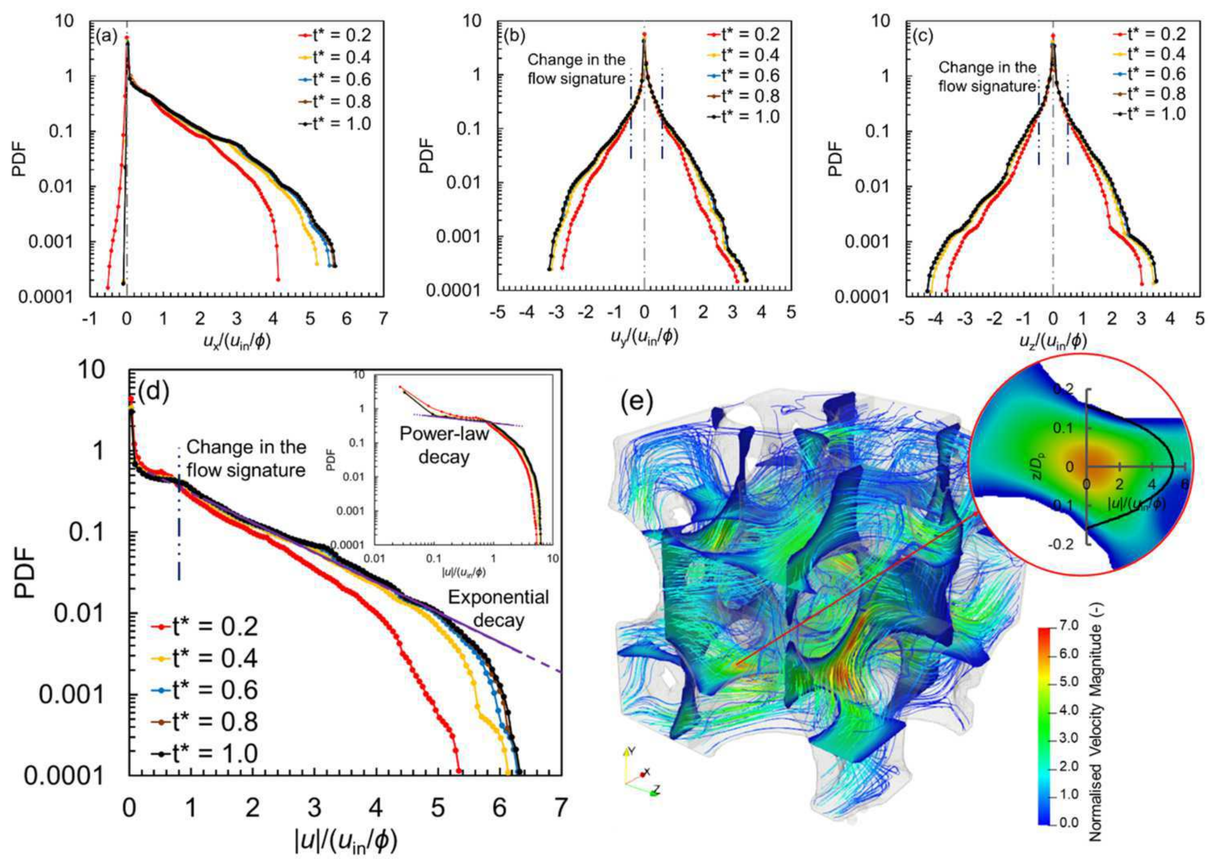
(a)
(b)
(c)
(d)
(e)
PDF
t* = 0.2
t* = 0.4
t* = 0.6
t* = 0.8
t* = 1.0
$u_x/(u_{in}/\phi)$
$u_y/(u_{in}/\phi)$
$u_z/(u_{in}/\phi)$
$|u|/(u_{in}/\phi)$
Change in the flow signature
Power-law decay
Exponential decay
z/D_p
Normalised Velocity Magnitude (-)

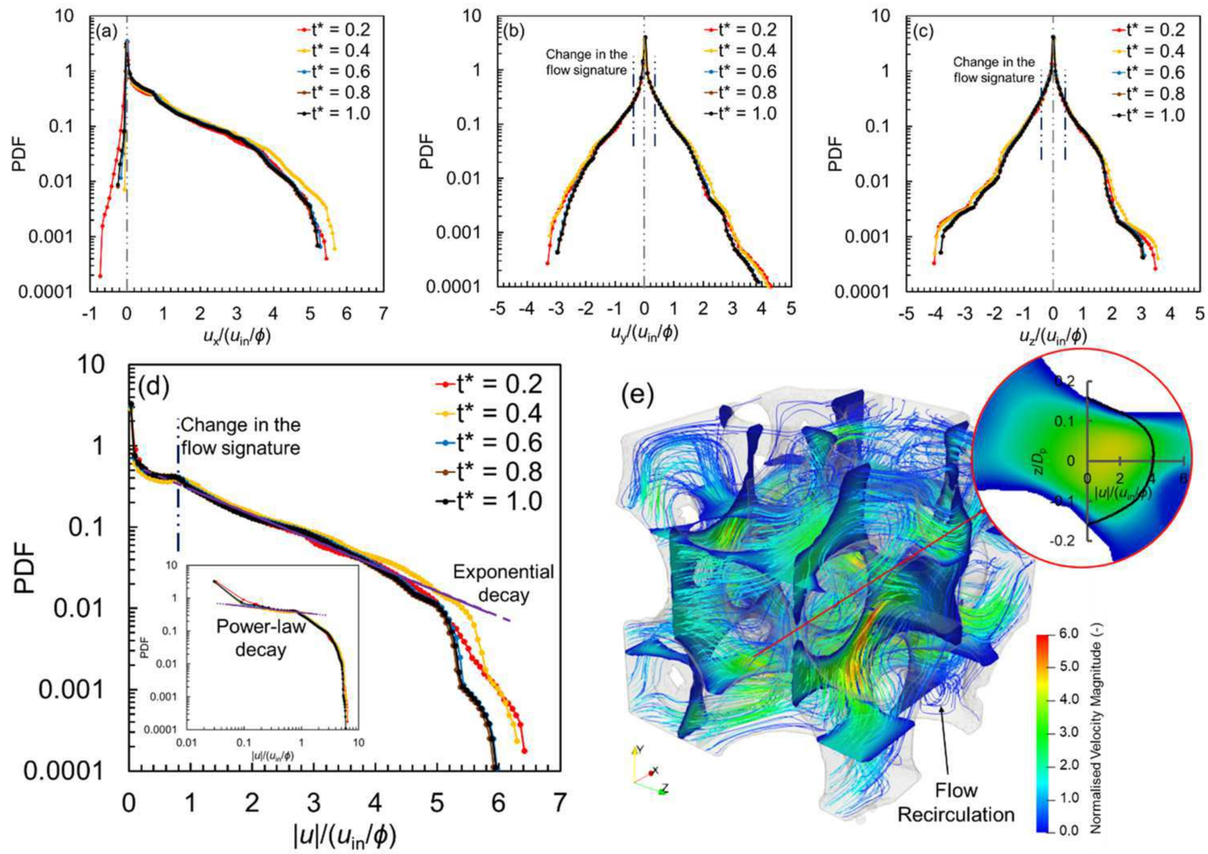
(a)
(b)
(c)
(d)
(e)
t* = 0.2
t* = 0.4
t* = 0.6
t* = 0.8
t* = 1.0
PDF
Change in the flow signature
Exponential decay
Power-law decay
Flow Recirculation
Normalised Velocity Magnitude (-)
$u_x/(u_{in}/\phi)$
$u_y/(u_{in}/\phi)$
$u_z/(u_{in}/\phi)$
$|u|/(u_{in}/\phi)$
z/D_p

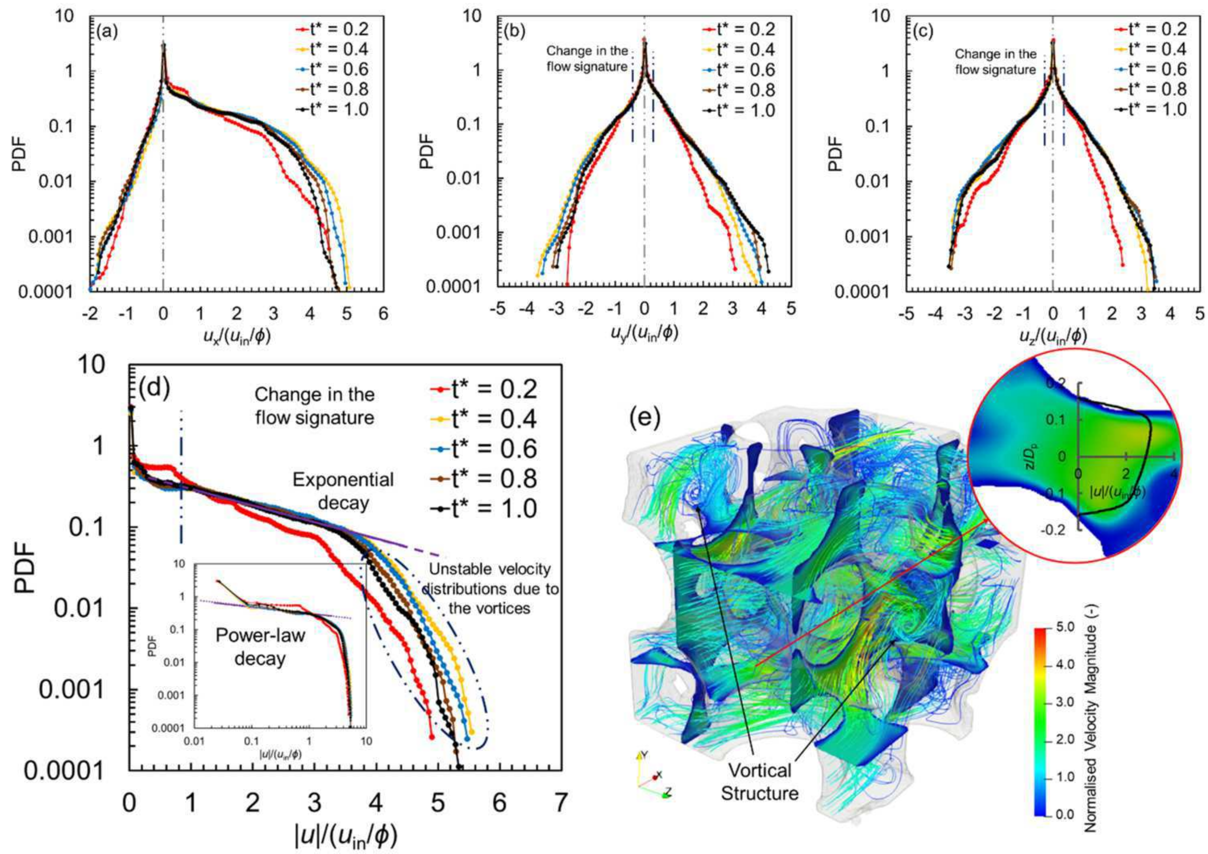
(a)
(b)
(c)
(d)
(e)
PDF
t* = 0.2
t* = 0.4
t* = 0.6
t* = 0.8
t* = 1.0
$u_x/(u_{in}/\phi)$
$u_y/(u_{in}/\phi)$
$u_z/(u_{in}/\phi)$
$|u|/(u_{in}/\phi)$
Change in the flow signature
Exponential decay
Unstable velocity distributions due to the vortices
Power-law decay
z/D_p
Vortical Structure
Normalised Velocity Magnitude (-)

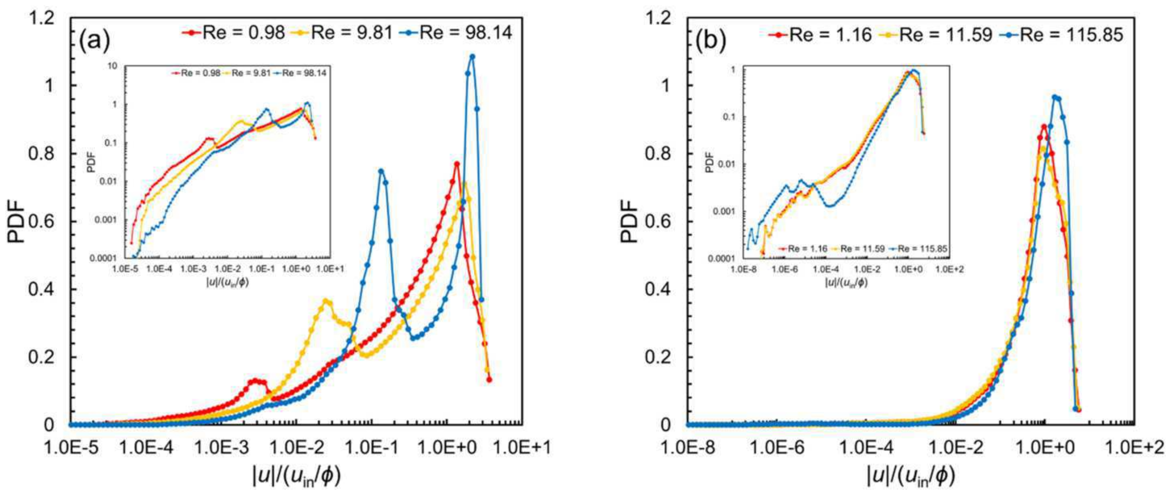
(a)
Re = 0.98
Re = 9.81
Re = 98.14
PDF
|u|/(u_in/ϕ)
(b)
Re = 1.16
Re = 11.59
Re = 115.85
PDF
|u|/(u_in/ϕ)

PLEASE CITE THIS ARTICLE AS DOI: 10.1063/5.0120201

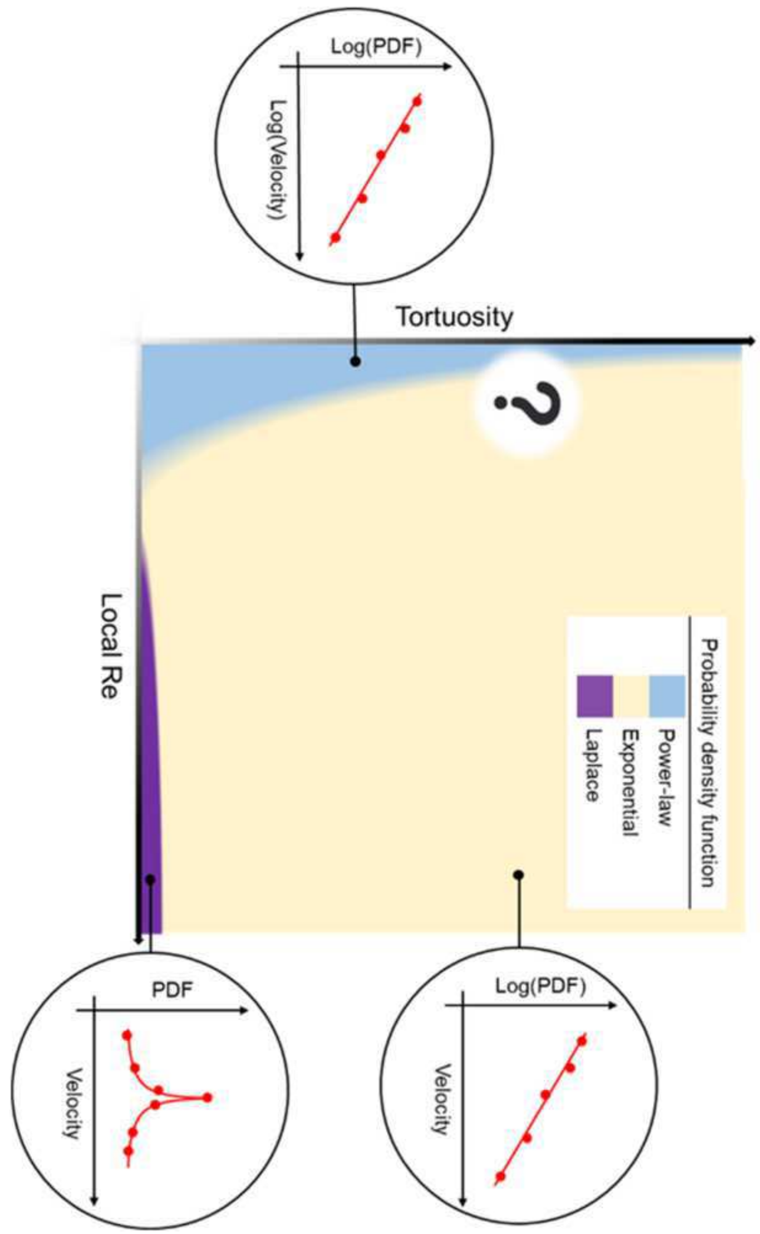

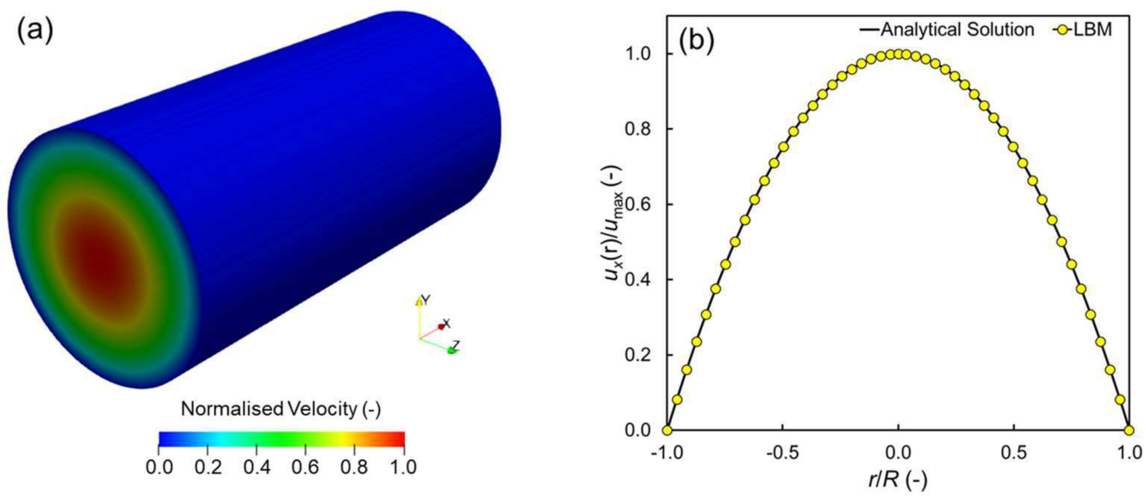
(a)
Normalised Velocity (-)
0.0 0.2 0.4 0.6 0.8 1.0
(b)
Analytical Solution
LBM
$u_x(r)/u_{max}$ (-)
r/R (-)
-1.0 -0.5 0.0 0.5 1.0
0.0 0.2 0.4 0.6 0.8 1.0